Composites: Part A 210 (2026) 110096

Contents lists available at ScienceDirect

Composites Part A

journal homepage: www.elsevier.com/locate/compositesa

Double-sided incremental forming of continuous fiber reinforced thermoplastics

Doran Nettig *, Jan-Erik Rath, Jon Ove Tiedemann, Thorsten Schüppstuhl

Hamburg University of Technology, Institute of Aircraft Production Technology, Denickestr. 17, 21073, Hamburg, Germany

ARTICLE INFO

Keywords:
Incremental sheet forming
Fiber reinforced plastic
Composite
Manufacturing process

ABSTRACT

Continuous fiber reinforced thermoplastics (CFRTP) combine excellent mechanical properties with recyclability, weldability, and reshapeability. However, their conventional processing requires part-specific tooling, imposing high initial cost and lead times. This limits their applicability to small lot sizes. A flexible alternative could be Incremental Sheet Forming (ISF), which creates parts by moving a small, part-agnostic tool along numerically controlled paths. While ISF is established for metals, its adoption for CFRTP started only recently. In particular, the Double-Sided Incremental Forming (DSIF) process, which employs a second forming tool to improve quality and flexibility, has not been investigated in detail for CFRTP. Therefore, this work presents the first extensive study into DSIF of CFRTP, with a focus on establishing a baseline process. The conducted process characterization includes temperature and force assessments. Forming strategies were compared by forming cone frusta, yielding a multi-stage strategy combining spiral and fiber-following toolpaths, which produced wrinkle-free parts with good accuracy. Micrographs indicate good consolidation for the tested material and process conditions. Furthermore, a preliminary process parameter analysis, including temperature, support force, and step size, was conducted. The results indicate that DSIF can become a viable, flexible manufacturing route for CFRTP components and provide a sound foundation for future research.

1. Introduction

The worldwide consumption of fiber reinforced plastics (FRPs) for the production of high-performance components across industries such as aerospace, automotive, sports equipment, and medical technology is increasing steadily [1]. Their high specific stiffness and strength make them attractive for applications that demand both lightweight design and mechanical reliability [2]. Among the various reinforcement fiber materials and architectures, woven continuous glass or carbon fiber fabrics are frequently favored due to their high reinforcing effect combined with relatively simple handling, good draping behavior, and wide availability [2]. Compared to classical thermoset resins, thermoplastic matrices have gained increasing popularity over the last years [1], as fiber reinforced thermoplastics (FRTPs) offer higher ductility, damage tolerance, weldability, reshapeability, and recyclability [2].

Due to the high viscosity of thermoplastic matrix materials, fully impregnated and consolidated organosheets are commonly used as semi-finished products. These sheets are then thermoformed into component-specific geometries with heated, part-specific molds [2]. While effective for series production, the associated tooling costs and lead times until production of the first part make this approach uneconomical for prototypes, individual parts, and small series [3]. This highlights the need for a more flexible forming process that does not require dedicated tooling.

One such solution could be incremental sheet forming (ISF), a dieless forming technology initially developed for metal sheets in the 1960s [4]. In this process, a simple standard tool, typically with a hemispherical tip, follows a programmed path, driven by a CNC machine or an industrial robot, to locally deform the circumferentially clamped sheet [5]. Three principal variants of the ISF process are distinguished in the literature, depicted in Fig. 1: Single Point Incremental Forming (SPIF) with just a single tool [6], Two Point Incremental Forming (TPIF) with a partial or full die on the opposite side of the sheet [7], and Double-Sided Incremental Forming (DSIF) using two opposing, coordinated tools [8]. Of the three process variants, DSIF provides the best combination of formability, flexibility, and part accuracy [9]. A DSIF setup with two opposing industrial robots was first introduced by Meier et al. [10]. Good workspace utilization, comparably lower investment costs, and high flexibility favor the use of robots over CNC machines in this case [10]. The drawback of lower stiffness can be mitigated by advanced path planning and force control techniques, including stiffness compensation [11]. While ISF is in an advanced stage for metals and has been adapted to some extent for thermoplastics [12–15],

* Corresponding author.
E-mail address: doran.nettig@tuhh.de (D. Nettig).

https://doi.org/10.1016/j.compositesa.2026.110096
Received 24 April 2026; Received in revised form 8 July 2026; Accepted 9 July 2026
Available online 20 July 2026

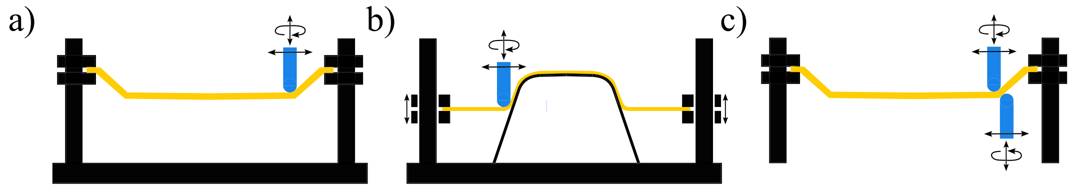

Fig. 1. Basic ISF process variants: (a) SPIF, (b) TPIF, (c) DSIF.

its application to continuous FRTPs is still at a comparably early stage of research [3,16]. This is primarily due to the fundamental differences in deformation behavior: whereas metals and thermoplastics, including those with short-fiber reinforcement, deform plastically through localized stretching and thinning [17,18], the deformation of continuous, and therefore also woven FRTP is dominated by the continuous fibers, which are nearly inextensible [19]. Thus, clamping them rigidly at the sheet edges as in standard ISF leads to fiber rupture [16]. Instead, the woven fabrics must be draped into the desired shape in a deformation process governed by bending, in-plane shear, and inter-ply sliding [19]. To address these challenges, early literature proposed a "floating" clamping configuration, in which the organosheet is attached to at least one metal dummy sheet while being allowed to slide relative to it. Fiorotto et al. [20] were among the first to apply incremental forming principles to fiber reinforced composites. Using a vacuum bag setup, they pressed a woven thermoset prepreg against a metal sheet, transferring the incremental deformation to the compliant fiber fabric. Xiao et al. [21] and Xu et al. [22] extended this approach by placing a rigid mold beneath the composite, thus realizing a TPIF-like configuration. Fiber draw-in and in-plane shear were identified as key deformation modes [21].

In addition to the special dummy sheet layup, woven FRTPs require heating the thermoplastic matrix above its glass transition or melting temperature to enable formability in ISF [23]. To this end, Al-Obaidi et al. [3] developed a setup in which the sheet layup is clamped atop an insulated chamber heated by a hot-air blower. A thin aluminum 5754 H111 sheet was used as a lower dummy sheet to prevent excessive heating and polymer melting. The upper dummy sheet was made of DC04 steel, protecting the woven glass fiber reinforced polycaprolactam (PA6) from direct tool contact. Polytetrafluoroethylene (PTFE) sheets were employed between the metal and organosheets to enable the sliding of the FRTP. SPIF was conducted with an NC machine, forming conical shapes with a depth of 20 mm. Especially at higher wall angles of 50 and 55°, wrinkles, folds, and internal defects such as cracks and voids developed. Results furthermore highlighted the need for homogeneous part heating [3]. Hou et al. [16] used a similar setup, employing a thermal radiation plate in an enclosed chamber to form woven jute-reinforced PLA. A backing plate was used to support the edge region of the formed pyramid with a wall angle of 45°. The maximum forming depth reached without failure was 20 mm [16]. Emami et al. [23] incorporated an infrared lamp for heating unidirectionally glass fiber reinforced PA6 sheets with comparably low fiber volume contents of 10 and 20% between two steel sheets. However, as the FRTP was clamped together with the metal sheets, fiber breakage occurred at forming depths higher than 18 mm, forming cones of up to 40° wall angle [23]. Mirnia Kalaei et al. [24] used the same general setup, forming truncated pyramids with 50° wall angle in woven glass fiber reinforced PA6 sheets with a maximum 30 wt-% fiber content. Again, the organosheets were clamped together with the dummy sheets, and a maximum forming depth of around 5 mm was reached [24]. In a numerical study, Ambrogio et al. [25] proposed the utilization of a pressurized and heated fluid instead of a lower dummy sheet, allowing for more homogeneous heating and pressure distribution on the FRTP.

The aforementioned SPIF-based approaches enabled the basic forming of FRTP but consistently led to defects such as wrinkles, cracks, and delaminations, limiting the achieved forming depth and wall angles. Notably, almost all prior work employed simple z-level or spiral toolpaths inherited from metal ISF, where the forming paths are based on the outer contours of the target geometry at equally spaced elevation levels [26]. Hou et al. [16] additionally investigated a toolpath that starts from the center of the sheet and moves outward in a spiraling motion at each z-increment, which led to slightly improved results. Also, Emami et al. [23] employed a multi-stage forming strategy, increasing the wall angle and depth of the part with each intermediate shape. However, those strategies neither account for the material anisotropy of continuously reinforced composites nor enable controlled draping of woven reinforcement fabric. The governing deformation mode necessary to accommodate double curvature in a woven fiber fabric is shear between the warp and weft yarns. This shear is typically introduced by in-plane tension along or across the fiber directions [27]. To address this limitation, Rath and Schüppstuhl [28] developed a drape-aware toolpath strategy for the incremental forming of woven FRTPs. The strategy uses a 3D tool motion aligned with the initial 0/90° fiber orientations, progressing from the center of the geometry outward. The sequence of the paths is chosen such that paths with a lower mean shear angle are formed first. SPIF experiments were conducted with the same general setup as in Al-Obaidi et al. [3], but using an industrial robot. Woven carbon fiber reinforced styrene-acrylonitrile (SAN) sheets with 45% fiber volume content were formed into cones with a wall angle of nearly 40° and 30 mm depth. The draping toolpath strategy yielded results with reduced fabric wrinkling compared to standard z-level strategies. However, due to the repetition of the inside-out toolpaths in each depth increment, tears occurred in the metal dummy sheets [28]. To improve and automate the strategy, we recently developed a fiber-following path planning algorithm that yields continuous drape-aware toolpaths based on an approximation of the fiber directions in the target part. To address the issue of an excessive number of intermediate shapes, the new algorithm was combined with a conventional elevation spiral approach in a path planning pipeline specifically developed for the ISF of FRP [29].

Even using a fiber-following strategy, an unsupported SPIF process still results in defects such as wrinkles and low overall part accuracy [28]. The use of a backing plate to support the edge of the formed cone has been shown to effectively address these issues, as it reduces global deformation and resulting deviations in the geometries of the two metal dummy sheets [28]. An option for providing controllable, flexible local support without introducing a part-specific backing plate is a DSIF system. A setup allowing the double-sided forming of woven thermoset prepregs was described by Xu et al. [30]. The single prepreg layer was sandwiched between two metal dummy sheets of different configurations, with only the metal sheets being clamped horizontally in a clamping frame. Forming was conducted by a CNC DSIF machine, producing cones with wall angles of 45° and 40 mm depth. Wrinkling and fiber breakage were the observed failure modes, with a configuration of 0.5 mm DC04 steel and 1 mm AA1050 aluminum as upper and lower dummy sheets, respectively, producing the best results [30]. For the DSIF of organosheets, the setup must additionally enable the global heating of the thermoplastic matrix while still allowing the movement of the support tool. The first such setup for the DSIF of FRTP was developed by the authors and is described in detail in a prior work [31]. It employs two synchronized industrial robots, one of which is force-controlled to provide a defined support tool force. An initial investigation of fiber-following paths using this setup showed promising results [29]. In this paper, the setup is leveraged for the first detailed study of the DSIF of woven FRTP. The setup and its components are briefly described in Section 2.2. The developed and utilized path planning algorithms, including the aforementioned drape-aware toolpath planning strategy, are explained in Section 2.3. Section 2.4 includes an explanation of the generated robot program and the force control algorithm. A series of experimental trials was conducted to identify a suitable forming strategy and evaluate in-process performance metrics, such as temperature and force homogeneity, and process outcome metrics, such as part accuracy, surface quality, and failure behavior. The experiments and analysis methods are described in Section 2.5. Finally, the results of the experiments are presented and analyzed in Section 3.

2. Materials and methods

In this section, the main steps of the process chain for robot-based double-sided incremental forming of continuous fiber reinforced thermoplastic sheets are elaborated, and the manufacturing system setup and materials used in the experiments are described. To focus the scope of this work on the DSIF manufacturing process, the process chain description spans all relevant steps after the design of a suitable target geometry and before any postprocessing operations, such as cutting, joining, or coating. The main inputs to the process were therefore the triangulated mid-surface of the target geometry and the sheet material described in Section 2.1. A sheet layup was prepared and subsequently moved to a clamping frame, where it was secured for forming on the developed setup, described in Section 2.2. On the digital side, the algorithms and procedures for preprocessing, path planning, and postprocessing are explained in Section 2.3. The resulting movement instructions were transferred to the robot controllers, and the forming process could start after heating the layup to the target temperature. The control architecture and the force-control algorithm employed for the support tool movements are elaborated in Section 2.4. The investigations for system characterization are described in Section 2.5.1, and the design of forming experiments follows in Section 2.5.2. For all forming experiments, the layup was cooled passively and removed from the clamping frame after a specified removal temperature was reached. Once cooled completely, the sheets were separated to retrieve the finished FRTP part, which was analyzed qualitatively and quantitatively as explained in Section 2.5.3.

2.1. Materials

As in previous publications described in Section 1, the continuous fiber reinforced composite sheet was quasi-floatingly interposed between two metal sheets, with additional separators to prevent adhesion between the composite and the metal. Only the metal sheets were clamped in the clamping frame to allow the fibers to be drawn into the formed geometry. Furthermore, the metal sheets maintain their shape even at elevated temperatures, aid in applying consolidation pressure to the composite, and prevent direct tool contact and damage to the FRTP. The layup used in this work is schematically shown in Fig. 2. The forming experiments in this work were conducted using commercially available Ensinger TECATEC SAN organosheets with two layers of twill-woven carbon fibers with a basis weight of 245 g/m^2. The resulting fiber volume content of the consolidated sheets with 0.6 mm thickness is 47 %. Samples were cut to 200 × 200 mm^2 and sandwiched between metal dummy sheets of 350 × 350 mm^2. DC04 steel of 0.7 mm thickness was used as the front dummy sheet in contact with the forming tool. The back sheet, in contact with the support tool, consisted of aluminum EN AW-1050 A H111 with a thickness of 1 mm. To separate the organosheet from the metal sheets, polytetrafluoroethylene (PTFE) sheets of 0.05 mm thickness and 350 × 350 mm^2 size were employed. Additionally, the PTFE allows for the sliding of the organosheet at a low coefficient of friction during forming. During layup, the aluminum sheet was placed on the bottom clamping bars, followed by a PTFE layer. The organosheet was then placed centrally on the PTFE layer, oriented so that the fiber directions corresponded to the sheet edges, and its corners were lightly secured to the PTFE layer using heat-resistant polyimide tape. Another PTFE layer and the steel sheet completed the layup, which was then secured by the upper clamping bars. To reduce friction between the metal sheets and the tooltips, a graphite and MoS_2-based solid lubricant spray was applied to the outer surfaces of the metal sheets before forming.

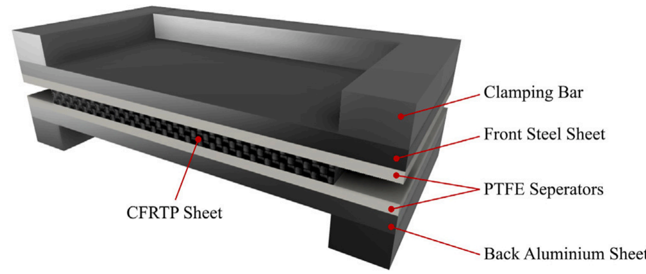

Fig. 2. Schematic depiction of the formed layup with the quasi-floatingly interposed continuous fiber reinforced thermoplastic (CFRTP) sheet and polytetrafluoroethylene (PTFE) separation sheets (depiction not to scale).

2.2. Manufacturing system

This work builds upon the previous conceptualization and design of a manufacturing system suitable for the hot DSIF of continuous FRTP in [31]. The solution enables the quasi-floating clamping configuration and heating of the organosheet in a force-controlled dual-robot setup. The physical structure of the system, displayed in Fig. 3, can be divided into four main subsystems. Namely, the *base platform* (orange), the *clamping system* (green) including the layup (blue), the *heating system* (red), and the *tooling* on both the hot side (rose) and cold side (yellow). These will be described in the following. The components of the *motion control system* are discussed in Sections 2.3 and 2.4.

The *base platform* consists of a steel platform, two six-axis industrial robots, and a steel frame. The subsystem realizes the fixed reference between the main system components, takes on the forming loads, and serves as the base interface for the other subsystems. The platform defines the footprint of the plant as 2.45 × 4.00 m^2. A KUKA KR 300 R2500 ultra and a KUKA KR 300 R2700-2 are mounted in the front right and back right corners of the platform, respectively. They have a repeatability of 0.06 and 0.05 mm, respectively, and both possess a handling capacity of 300 kg. The robot stiffnesses of this specific plant have not yet been determined. However, research on incremental forming with KUKA KR340, a similar handling weight class, showed a force-dependent displacement of 0.0015 mm/N [11]. The permissible flange loadings during operation exceed 5 kN in the axial and 4.5 kN in the radial direction. The top truss, bottom rail, and the central H-assembly of the steel frame allow for flexible positioning of the clamping system. The configuration in this work keeps the H-frame on the side opposite to the robots to mitigate robot singularities. The frame is built from 100 × 100 × 5 EN 10219 S235JRH beams, ensuring a maximal deflection of less than 0.1 mm at expected forming loads of 3 kN.

The *clamping system* employs a two-step approach. First, the layup is manually prepared on a horizontal layup table as described in Section 2.1, and clamped by the clamping strips via hand-bolted connections. Handles are attached, and the layup is moved to the clamping frame, where it is secured by toggle clamps. In this work, the clamping frame was used in its smaller configuration with a 325 × 325 mm^2 window. To reduce stresses from constrained thermal expansion, the

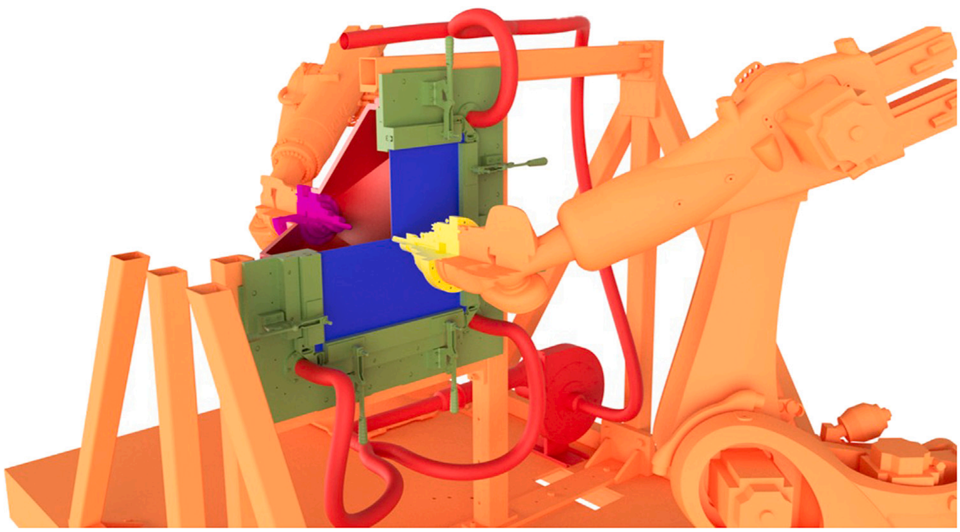

Fig. 3. The physical Hot-DSIF system with colored subsystems: base platform (orange), clamping system (green), layup (blue), heating (red), hot tool (rose), cold tool (yellow).

toggle clamps and screws are loosened during heating. After reaching the target temperature, the screws are hand-tightened again, and the toggle clamps are fully closed.

To heat the layup, the *heating system* uses a Leister LE 10000 DF-R heater with a maximum power of 11 kW in conjunction with a Leister RBR radial blower with a nominal volume flow rate of 175.8 ls^{-1}. This setup circulates hot air in the bespoke heat-resistant bag, which has an inner liner with a heat resistance rating of 500 °C, an insulating layer, and an outer layer with a heat resistance of up to 450 °C. The bag connects the clamping window and the support tool to form a flexible oven chamber on the back of the layup. Hot air enters the chamber through two inlets on the bottom corners and is redirected towards the layup by two deflection sheets. Insulating material reduces heat transfer into the clamping frame, focusing the heat on the layup. The hot air is recirculated through two outlets on the top corners of the chamber. While the airflow rate remains constant during operation, the heat input of the DF-R is PID controlled, taking the measurement of a type K thermocouple placed inside the heated chamber halfway between the in- and outlet on the left edge of the clamping frame as control input. The entire system is designed to withstand internal temperatures up to 350 °C. However, in this study, the temperature range is limited to a maximum setpoint of 180 °C.

The *tooling* differs slightly between the two robot end-effectors. Both employ a cylindrical tool insert with a dome-shaped tip made from hardened 1.2210 steel. The tool inserts used in this work have an exposed length of 80 mm and a 20 mm dome diameter. In this configuration, both tools show an overall clearance angle of about 70°. Each tool is connected to the respective robot end-effector via a six-axis force–torque sensor. The cold forming tool on the front side uses a Schunk FTN-Omega-191, and the hot tool on the backside support robot uses a Schunk FTN-Omega-160. The reason for this differing sensor choice is their differing primary function as guiding and supporting robots, which will be further explained in Section 2.4. Aside from the sensor choice, another difference results from the back robot operating at the interface between the cold environment and the heated chamber. This necessitates the use of a cooling coupler that shields the sensor from any potential heat influx. The cooling coupler is a water-cooled adapter that dissipates heat from the hot tooltip using a TEYU CW-5200 industrial water chiller with a cooling capacity of 1.43 kW and a temperature stability of ±0.3 °C.

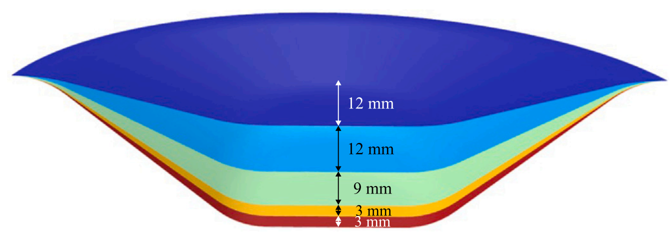

Fig. 4. Intermediate shapes generated through the preprocessing pipeline by linear height interpolation with the maximum distance to their respective predecessor.

2.3. Path planning

Path planning is an important element of the incremental forming process. This work uses the drape-aware and elevation-based spiral toolpath algorithms described in [29] and extends them with another conventional spiral algorithm. Instead of a constant elevation, this second approach achieves a constant scallop width spiral strategy, which is also commonly used in ISF, although the algorithm as implemented here differs slightly from previous approaches. This section describes the entire path planning pipeline used in the experiments of this work. For additional details on the implementation, the interested reader is referred to the aforementioned publication.

Independent of the path planning algorithm used, the input geometry is first remeshed and transformed, if necessary. To enable multi-stage forming strategies, the desired intermediate shapes with user-defined layer distances d_l are generated via elevation field interpolation. An example of intermediate shapes produced by this pipeline is shown in Fig. 4. The example shows five linearly interpolated intermediate shapes of a cone frustum, including the final shape (red).

For the spiral path strategies, the isolines of a scalar field are connected into continuous spirals. This scalar field can simply be the height field of the geometry, given by the z-coordinate of each surface point. The resulting elevation-based spiral paths are shown in Fig. 5(a). While this algorithm and the general pipeline have already been elaborated and used in [29], this work extends the concept by constant scallop width spirals. For the implementation of such spirals, Lu et al. [32] proposed an algorithm based on separating the geometry into features with distinct boundaries and the pointwise calculation of the Euclidean distance to these boundaries. The algorithm described here instead

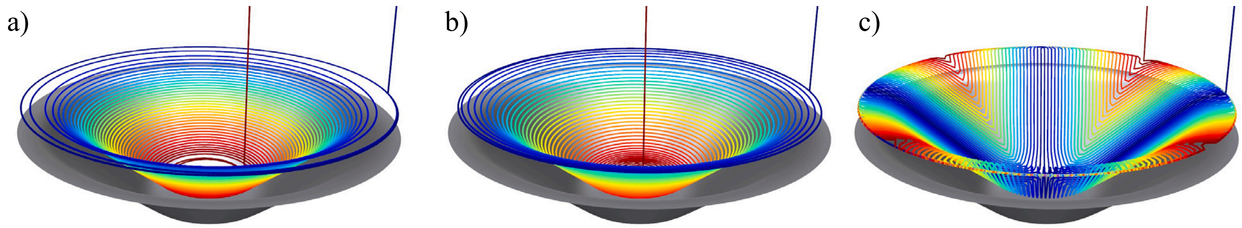

Fig. 5. Different path types generated by the path planning pipeline: (a) elevation-based spiral, (b) geodesic distance spiral, (c) fiber-following paths.

leverages the heat method for generalized signed distance originally introduced by Feng and Crane [33] for the efficient calculation of the geodesic distance field from the boundary. This heat method uses the diffusion of a vector field at a source curve to efficiently compute the signed geodesic distance from that curve. In the case of the constant scallop width spirals, this distance corresponds to the shortest piece of yarn that would connect a given point to the boundary, while also being placed entirely on the target surface. Using the heat method instead of pointwise Euclidean distances has the advantage of producing isolines that have equal distances on the part surface, being applicable to arbitrarily shaped geometries without the need for feature extraction and remaining computationally efficient. Still, the computation also starts by identifying the outer contour of the overall part geometry by point connectivity. The outer edge is iteratively sorted starting from an arbitrary point, and the resulting sorted polyline is used as input to compute the signed geodesic distance field. The resulting scalar field of signed distances can now be used analogously to the height field. Its isolines are extracted and spiralized to obtain the constant scallop width spiral shown in Fig. 5(b). On a side note, the set of boundary points could directly be used as the source for an unsigned geodesic distance computation [34], which is even more computationally efficient. However, this requires using a mesh that is fine compared to the chosen contour distance to avoid numerical issues close to the boundary. To make the algorithm more robust, the signed heat method is used instead, as it is still very fast in its computation.

Previous publications have demonstrated the potential of fiber-following paths to reduce wrinkling defects in the SPIF and DSIF of woven FRTP [28,29]. In this work, the fiber-following path planning algorithm developed in [29] was applied as well. It uses an equidistant approximation of the fiber tow locations in the deformed geometry to plan paths. The resulting toolpaths follow the approximated fiber directions while also having constant scallop width. In the configuration used here, the paths start at a central fiber cross defined by a chosen origin, dividing the shape into four quadrants. From this cross, further paths are added into the quadrants. This means the tool globally moves from an area of low shear, i.e., the central fiber cross, where fibers mostly bend, to one of high shear. The paths are connected along the shortest distance on the boundary to form a continuous path. An illustration of the resulting paths is shown in Fig. 5(c), with the path progress being colored from start (blue) to finish (red).

After generating the paths, they are postprocessed to add necessary approach and retract movements and to offset them based on the tool diameter and material thickness. Lastly, the path points are used to generate the robot instructions explained in Section 2.4 using a custom parser.

2.4. Robot instructions & force control

Building on the paths generated as described in the previous section, this section focuses on the digital aspects of the robotic system. It covers the general concept of the robot synchronization, the force control of the supporting robot, and the path routines. One similar robot setup in the existing literature on metal DSIF is that described by Möllensiep et al. [11]. They employed two KUKA robots in time-synchronized coordination mode, with a force-control algorithm implemented on the support robot's controller that relies on precomputed relative positions of the two robots. Furthermore, they integrated an external stiffness compensation algorithm, which is not yet employed in the hot DSIF setup described here. Aside from the stiffness compensation, the main difference is that the setup presented here uses geometric coupling combined with time synchronization for the coordination of the two robots, as a KUKA-native control option. In this setup, one robot is designated as "Master" (referred to as the guiding robot in the following) and one as "Slave" (referred to as the supporting robot in the following). The base frames of both robots are linked, and during path execution, the supporting robot continuously queries the tool center point (TCP) position of the guiding robot, which it uses as a moving workpiece coordinate system. Relative movements in the TCP frame of the guiding robot are then additionally time-synchronized with the movements of the guiding robot. While this approach is limited to a 12 ms cycle time, it allows for the direct creation of the relevant geometric link between the guiding and supporting robots instead of implicitly creating it through two workpiece frames with known relation and precomputed relative tool positions. A further advantage is the more reactive force control, as the information on the relative position of both robots is directly available in every interpolation cycle, rather than at the path-point level.

Conceptually, the force controller follows the same principle as the approach described by Möllensiep et al. [11], but is adapted to the coupled approach described in [31]. The general controller layout, as implemented using the KUKA Robot Sensor Interface (RSI), is shown in Fig. 6. Monitoring, safety, and signal exchange functionalities are omitted in this diagram. The force controller is implicit, adjusting the distance between the guiding and support robot TCPs in response to the force error. The implementation in this work computes the dot product of the normalized current position P_{act} of the support robot and the current force measurement transformed to the robot's TCP, F_{mes}, to obtain the force component pointing from the supporting to the guiding TCP. The target force is subtracted, yielding the force error, which is then scaled by a limited PD-Element to obtain the incremental position correction ΔL_{corr}. Next, this incremental correction is turned into the total position correction for the next time step L_{corr}. This is implemented by first obtaining the new total tool distance $L_{total} = \|P_{act}\| + \Delta L_{corr}$ of the current time step and then subtracting the norm of the current commanded position $P_{cmd} = P_{act} - P_{corr}$, with P_{corr} being the current total correction vector. The length of the new total correction $L_{corr} = L_{total} - \|P_{cmd}\|$ is then transformed back to 3D space by multiplying it with the normalized commanded position vector of the current time step to obtain the correction vector for the next time step $P_{corr} = L_{corr} \frac{P_{cmd}}{\|P_{cmd}\|}$. Finally, this total correction is applied to the robot. Within the pipeline, two filters are applied to reduce noise amplification. The initial force signal is filtered with a second-order lowpass Bessel filter with a cutoff frequency of 10 Hz, and the input to the differential component of the PD-Element is further filtered with a 5 Hz cutoff frequency. The values chosen for the PD-Element are P = 0.00015 and KD = 0.000002 with upper and lower output limits of 0.04 and −0.02, respectively. The 12 ms interpolation cycle requires an absolute position correction as input for the KUKA-native *PosCorr* function as opposed to a relative correction. This, in turn, necessitates

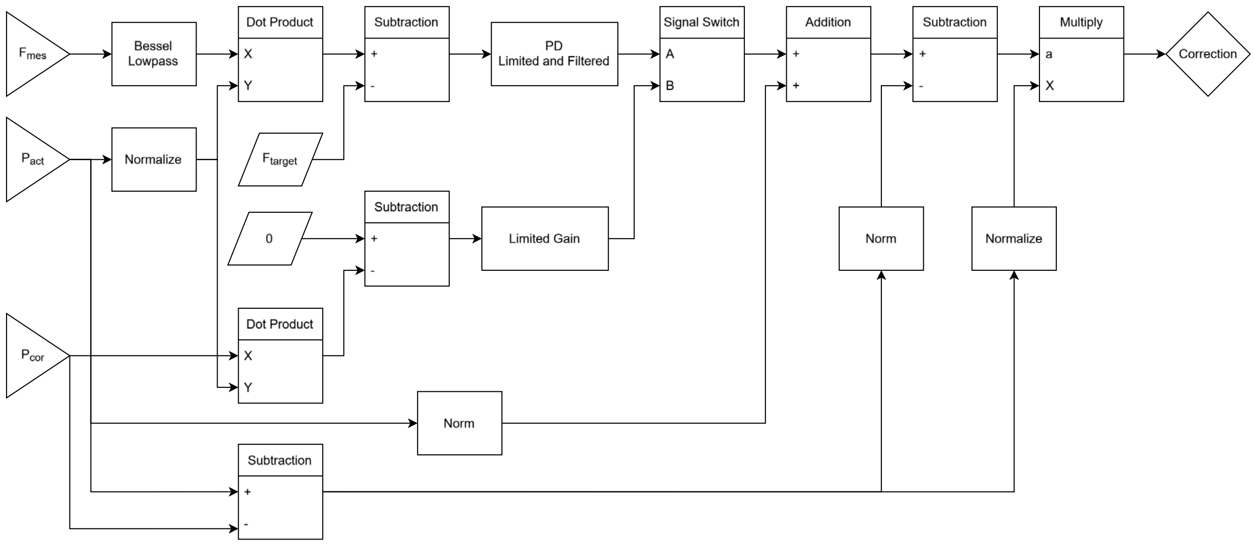

Fig. 6. The working principle of the system's implicit force-controller.

switching the controller to an incremental reduction of the correction once the final path point is reached, rather than simply switching it off. This incremental reduction is implemented as a P-Controller with the length of the position correction as the error variable. The gain of the P-Element for removing the position correction employs a Kp of 0.002 at limits of ±0.004. During all movements, including those in which the robots are not forming, the corresponding force and torque measurements are monitored, and the process is stopped if certain limits are exceeded. This serves as an additional safety precaution to prevent damage in case of erroneous robot positions or critical part failure.

Aside from the force monitoring and control, executed by the RSI, the robot movements are defined in KUKA Robot Language (KRL) files generated by the path planning system described in Section 2.3. Both robots start in their respective home positions. First, the guiding robot moves its forming tool to the initial path point and waits there. Next, the supporting robot approaches its initial point on the back of the layup. This initial point is programmed with a specified offset, such that contact is established only when the force controller is engaged. It incrementally reduces the distance between the guiding and support tools until the target force is reached. Only then do the actual forming movements begin. The path is then formed with a mostly constant velocity of 20 mm/s (the TCP speed of the guiding robot). By setting the TCP speed of the supporting robot to 5 mm/s (its relative velocity within the moving frame of the guiding robot's TCP), the total speed is reduced if significant relative motion of the supporting tool occurs within a comparatively short global path segment. Once the path is completed, the supporting robot retracts to a specified point while simultaneously reducing the position correction. After reaching the retract point and switching to a fixed base coordinate system, the guiding robot returns to its retract point, and the process can continue with the next shape.

2.5. Design of experiments and analysis methods

As this work presents the first investigation into the DSIF of FRTP, the experimental analysis focused on characterizing the process and an initial identification of a suitable process strategy and parameterization. A more elaborate process optimization based on a comprehensive statistical design and analysis of factor effects and interactions was explicitly out of scope and left for future investigations. However, the goal was to enable the design and interpretation of subsequent investigations by identifying a suitable starting point and a well-characterized reference.

2.5.1. System characterization

To characterize the system and the process, several descriptive analyses were carried out, allowing comparison with other variants and possible future implementations. One aspect in this regard is the forming force. The forces acting on the end effectors were measured with a Schunk FTN-Omega-191 SI-3600-700 on the guiding robot and a Schunk FTN-Omega-160 SI-2500-400 on the support robot. Both forces and moments were continuously recorded during the forming process, with axial and radial force resolutions of 1.5 N and 0.75 N for the guiding robot, and 0.75 N and 0.5 N for the support robot.

First, to determine potential effects of temperature fluctuations associated with the heating and cooling systems, the stability of the force measurements was assessed. This was done by recording the output of both force–torque sensors during an experiment in which the robots remained in their home positions. The forces were zeroed at the start of the heating period and subsequently recorded for one hour. The target temperature of the chamber was set to 180 °C during this experiment. Next, the performance of the force controller was assessed by replicating a trial of Möllensiep et al. [11]. The formed geometry and the forming parameters were identical to those of experiment number 30 in [11], to which the results were compared. Therefore, a 0.7 mm DC04 steel sheet was formed with a speed of 20 mm/s. An elevation spiral toolpath was used with a contour distance of 0.5 mm. The target support force was set to 200 N. For this experiment, the limit on the relative support robot velocity and the graphite lubrication were removed. Finally, the forces in the forming process were analyzed exemplarily during two of the forming experiments described in Section 2.5.2, experiments 10 and 11 in Table 1. The support robot measurements served to assess the characteristics and performance of the force controller during the actual CFRTP forming. The measurements of the guiding robot, on the other hand, enabled the analysis of the forming forces.

To assess the homogeneity and accuracy of the sheet temperature, a heating experiment was conducted, employing both global thermographic and local thermocouple measurements. A complete layup of steel, PTFE, FRTP, and aluminum sheets was heated, with the target temperature of the chamber set to 180 °C. After reaching the target temperature, it was kept constant for 90 min. Subsequently, the target temperature was reset to zero, and the cooling ramps were recorded for an additional hour. The temperature distribution in the plane was measured with a FLIR A5 infrared camera, which requires a non-reflective coating of the outermost metal sheet. Four markings were kept uncoated that indicated the outer dimensions of the 200 × 200 mm^2 organosheet within the layup. The internal temperature of the chamber

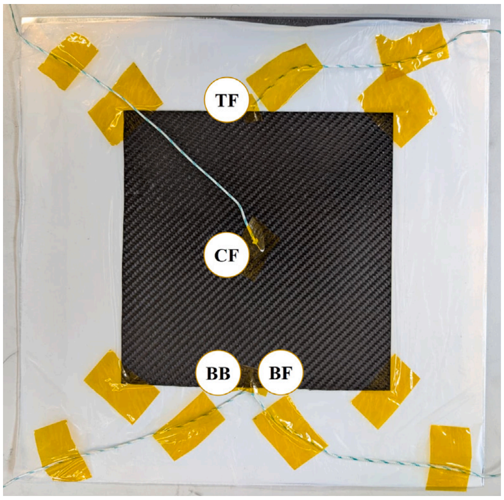

Fig. 7. Locations of type K thermocouples: BF (bottom front), TF (top front), CF (center front), and BB (bottom back).

and several positions within the layup were measured with type K thermocouples. The positioning of the local measurement points on the organosheet is shown in Fig. 7. The locations are named by their position in the clamped layup. Three sensors were placed on the outer side of the organosheet facing the guiding robot, referred to as the "front", and one was placed on the side facing the heated chamber, referred to as "back", to assess the through-thickness temperature gradient. One of the front sensors was placed in the center of the sheet. To assess the in-plane temperature gradient, the other two front-facing sensors were placed on opposing edges of the sheet, the top and bottom locations in the vertical clamping frame. The back-facing sensor was placed at the bottom as well. The locations are abbreviated in the following as BF (bottom front), TF (top front), CF (center front), and BB (bottom back).

2.5.2. Forming experiments

The main investigative focus of this work is the exploratory identification of a suitable forming strategy, particularly in light of the novel path planning algorithms. Therefore, several strategies were compared by forming a cone frustum with a 40° wall angle, as shown in Fig. 8. The notation of the different forming strategies, as in Table 1, consists of an identifier for the employed path strategy (E: elevation spiral, G: geodesic spiral, D: draping/fiber-following strategy), followed by the forming depth (relative to the previous shape) in mm, rounded to the next integer value. Consequently, the conventional one-shot elevation spiral strategy used as the baseline is denoted E40. It was compared with several strategy combinations based on the algorithms described in Section 2.3. Within these combined strategies, the final cone geometry was reached via multiple intermediate shapes. The intermediate shapes are defined by their maximum distance to the previous stage as explained in 2.3. In the notation used here, the different forming stages are separated by a hyphen (-). Thus, a multi-stage strategy denoted E10-E10-E10-E10 consists of four intermediate shapes, each with a maximum separation of 10 mm, adding up to the final depth of 40 mm. After comparing the single-stage E40 (experiment ID 03) and multi-stage E10-E10-E10-E10 (ID 04) strategies, the effect of forming the final shape with a draping toolpath was investigated in strategy E12-E12-E12-D3 (ID 05), maintaining the total number of four intermediate shapes. The E12-E12-E12-D3 (ID 06) and E12-E12-E9-D3-E3 (ID 08) strategies served to investigate whether an additional final finishing spiral toolpath with a low depth increase could improve the process outcome without introducing new wrinkles. Furthermore, E10-E10-E10-E10-D0 (ID 09) was used to analyze the effect of the

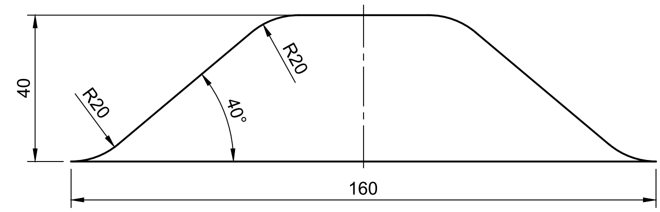

Fig. 8. Dimension of the cone frustum geometry used for the conducted experiments (all measurements in mm).

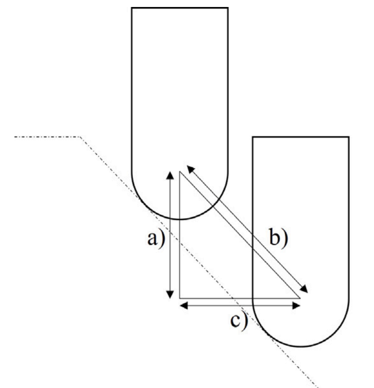

Fig. 9. Different step size metrics: (a) vertical step down, (b) scallop width, and (c) horizontal step size.

depth and position of the draping toolpath in comparison with both aforementioned strategies, as well as with E10-E10-E10-E10. Additionally, the effect of a cooling run was studied, i.e., repeating the last shape while reducing the forming temperature, in a strategy denoted E12-E12-E9-D3-E3-E0c (ID 10). During the cooling run, the speed was manually reduced to 50 %. Lastly, the use of elevation-based spirals was compared to that of geodesic spirals with the G12-G12-G9-D3-G3-G0c strategy (experiment 11). For all strategies, both robots were stopped at the end of the last shape until the removal temperature of 60 °C was reached. This was intended to suppress the springback of the global elastic metal sheet deformation while the organosheet was still malleable. Otherwise, the springback would likely transfer to the organosheet, and the different elastic moduli of steel and aluminum sheet might cause a severe separation and loss of compaction.

In addition to analyzing different process strategies, an initial investigation of basic parameter influences was conducted. Among the experiments, the parameters temperature setpoint, support force, front sheet material (combined with thickness), and step size were varied. This was done in conjunction with the strategy experiments, following a simple one-factor-at-a-time procedure. The temperature setpoint was varied between 150 and 180 °C, employing the E40 strategy (experiments 01 vs. 03). Using the E12-E12-E12-D3 strategy, the force was varied between 150 and 200 N (IDs 05 vs. 06), and the front sheet was switched from a 0.7 mm DC04 steel sheet to a 1 mm 1050 A H111 aluminum sheet (experiments 06 vs. 07). The step size needs to be interpreted slightly differently between the elevation strategy, where it was synonymous with the step down, and the geodesic and draping strategies, where it represents the scallop width. This difference is illustrated in Fig. 9. To account for this difference, the step size was set to 1 mm for the elevation strategy and doubled for the latter two strategies. It was explicitly varied at the G12-G12-G9-D3-G3-G0c strategy between 2, 3, and 5 mm to investigate its effect (experiments 11, 12, and 13). To evaluate the role of the supporting robot and the transferability of the results to the SPIF of woven FRTP, the conventional E40, as well as the G12-G12-G9-D3-G3-G0c strategies were used

Table 1
List of the performed experiments.

ID	Front sheet	Force [N]	Temperature [°C]	Step size [mm]	Method	Strategy
01	0.7 mm DC04	150	150	1	DSIF	E40
02	0.7 mm DC04	0	180	1	SPIF	E40
03	0.7 mm DC04	150	180	1	DSIF	E40
04	0.7 mm DC04	150	180	1	DSIF	E10-E10-E10-E10
05	0.7 mm DC04	150	180	S1/D2	DSIF	E12-E12-E12-D3
06	0.7 mm DC04	200	180	S1/D2	DSIF	E12-E12-E12-D3
07	1 mm Al-1050 H111	200	180	S1/D2	DSIF	E12-E12-E12-D3
08	0.7 mm DC04	200	180	S1/D2	DSIF	E12-E12-E9-D3-E3
09	0.7 mm DC04	200	180	S1/D2	DSIF	E10-E10-E10-E10-D0
10	0.7 mm DC04	200	180	S1/D2	DSIF	E12-E12-E9-D3-E3-E0c
11	0.7 mm DC04	200	180	2	DSIF	G12-G12-G9-D3-G3-G0c
12	0.7 mm DC04	200	180	3	DSIF	G12-G12-G9-D3-G3-G0c
13	0.7 mm DC04	200	180	5	DSIF	G12-G12-G9-D3-G3-G0c
14	0.7 mm DC04	0	180	5	SPIF	G12-G12-G9-D3-G3-G0c

to form a part with the support robot disabled, comparing the results to DSIF (experiments 02 vs. 03 and 13 vs. 14). A complete list of all described experiments is found in Table 1. Given the experiments' exploratory intent, they have neither been randomized nor repeated. Still, an initial assessment of the importance of parameter interactions and the repeatability of the identified process setpoint was carried out. To achieve this, the theoretically best process setpoint identified from the experiments was used to parameterize a final fifteenth experiment, which was then performed three times.

To give an overview of all experimental parameters and factors, the parameter classification developed in [35] is used. It is shown in Table 2, with parameters to be determined during the experiments marked in yellow (cooling ramps, maximum sheet temperature, and temperature distribution) and parameters that were varied across experiments marked in green. The exact machine stiffness and clamping force were unknown during the experiments. The machine stiffness is highly configuration and direction-dependent and was only roughly estimated within the scope of this work. The clamping process was carried out by hand-tightening screws, which also introduces uncertainty about this parameter. Both values are therefore marked red to highlight these uncertainties.

2.5.3. Analysis methods

The process and its outcomes were analyzed with respect to formability criteria, quality metrics, and process targets. Formability was assessed by categorical and qualitative visual inspection for tearing of metal, separator, and composite material, and for severe wrinkling in the composite and PTFE separator sheet. Additionally, the failure modes of deconsolidation and delamination were assessed alongside the microstructural quality metrics described later. The main quantitative quality metric was the geometric deviation of the formed composite part from the target geometry. The parts were scanned with a GOM ATOS Compact Scan 5M 3D scanning system after complete cooling to room temperature and removal from the layup. They were placed on a flat surface with the tip of the cone frustum pointing up. After scanning and triangulating the as-is geometry in ZEISS Inspect 2023, the same software was used to load an STL model of the target geometry, perform an initial best-fit alignment with the scanned geometry, and compute a surface comparison showing the pointwise deviation between the scanned and target geometries. The deviation field was qualitatively assessed regarding the extent and distribution of the deviation. Additionally, to guide the quantitative assessment, four accuracy metrics were computed: the minimum, maximum, and spread of the error, as well as the standard deviation of the error distribution. While this best-fit alignment does not provide the same absolute reference as an alignment in the clamped state, it is a commonly used and practical procedure for ensuring consistent and automated comparison of geometries when scanning in the clamped configuration is not feasible. Due to the low thickness and curved geometry of the investigated parts, samples for mechanical tests, such as inter-laminar shear stiffness or tensile strength, could not be cut from the formed parts. An additional set of experiments using geometries specifically suited for such tests would exceed the scope of this work. The influence of process parameters on the mechanical properties of the resulting parts, therefore, has to be investigated in future research. Void geometry and the occurrence of cracks were investigated as quality metrics of the microstructural consolidation state. The analysis was performed using cross-sectional micrographs obtained with a Keyence VHX-X1 digital microscope. Because of the additional steps of cutting, embedding, and polishing cross sections, the consolidation assessment was limited to one part produced with the same parameters as in experiment 11, one part formed with the same parameters as in experiment 3, and two virgin material plates. To obtain the samples, strips were cut from the middle of the sheets, perpendicular to the fiber directions. For the formed cones, three 27–30 mm long sections were cut from the resulting strips. The three sections were cut from the base radius, wall, and tip radius of the formed cone frustum, respectively. For the virgin material, one section was cut from a random location in each of the strips. An ATM Brillant saw with a water-cooled corundum blade was used for all cuts. Subsequently, the samples were embedded and polished. All examined target variables and the measurement methods employed are summarized in Table 3, following the classification developed in [35].

3. Results

3.1. Temperature analysis

The results of the temperature analysis reveal several properties of the heating system, including the heating and cooling ramps, in-plane temperature homogeneity, and the through-plane temperature gradient. The data recorded from the thermocouples placed within the layup is plotted in Fig. 10. The target temperature inside the chamber of 180 °C was reached after 20 min and remained nearly constant for the remaining 90 min until cooling. At this point, the temperature within the layup had reached 90–110 °C, depending on the measurement position. The temperature within the layup also mostly plateaued after the target chamber temperature was reached. However, a slight slope remained until heating was shut off. The glass transition temperature of the SAN matrix of 110 °C was exceeded at all measurement locations about 60 min after the start of the heating. At the end of the heating period, the temperature was at its maximum of 115–128 °C within the layup. The significant deviation from the chamber temperature of 180 °C can be attributed to the insulating effect of the layup components and to heat dissipation from the front steel sheet to the environment. The temperature differences within the layup were considerably smaller. While the top and bottom temperatures were very similar, with a mean difference of only 1.45 °C between BF and TF, the center of the layup was approximately 15 °C hotter than the perimeter, as could be expected. The through-thickness temperature gradient was measured to be about 3.4 °C (BB-BF), which is likely a result of the low

Table 2
List of all set and varied parameters following the characterization proposed in [35].

Platform					
Machine		Fixture and heating		Tool	
Axis Config	2RRRRRR	Backing plate details	No backing plate	Tool coating	None
Forming method	SPIF/DSIF	Clamping geometry	315 × 315 mm^2	Tool material	1.2210
Load capacity	300 kg	Clamped components	Metal sheets and separator	Tool shape	Hemisphere
Machine stiffness	approx. 0.0015 mm/N	Type of heating	One side convective	Tool size	D = 20 mm
Machine type	Industrial robots (KR300 R2500/R2700)			Tool type	Fixed tip
Position repeatability	±0.06 mm				
Work space size	2.5 and 2.7 m reach				
Process					
Path and motion		Temperature and lubrication		Force and pressure	
Feed rate	20 mm/s	Lubrication type	Graphite and MoS_2	Back side pressure	None
Forming orientation	Vertical	Application method	Spray	Clamping force	Hand-tight. M8 Hex
Forming strategy	Single stage, multi stage	Application frequency	Once	Front pressure	None
Spindle direction	Fixed	Heating ramps	TBD	Support angle	0°
Spindle speed	0 rpm	Cooling ramps	TBD	Support force	0, 150, 200 N
Step size	1, 2, 3, 5 mm	Max. chamber Temp.	150, 180 °C		
Superimposed shape	None	Max. sheet Temp.	TBD		
Toolpath direction	Clockwise	Temperature distribution	TBD		
Toolpath type	Elevation spiral, geodesic spiral, fiber-following				
Product					
Material		Geometry			
Front sheet material	Steel DC04, aluminum EN AW-1050A H111	Front sheet thickness	0.7, 1 mm		
Back sheet material	Aluminum EN AW-1050A H111	Back sheet thickness	1 mm		
Separator material	PTFE	Separator thickness	0.05 mm		
Fiber material	Carbon fiber	Fiber geometry	HT 3k tow		
Reinforcement type	Woven	Input sheet geometry	200 × 200 mm^2		
Reinforcement details	Uniform twill weave	Initial sheet thickness	0.6 mm		
Fiber orientation	0/90	Part shape	Cone		
Anisotropy	0/90	Symmetry	Rotational		
Area weight (fibers/sheet)	245/411 g/m^2	Geometry features	None		
Matrix material	SAN	Part dimensions	D160 × H40		
Preform fabrication	Double belt press	Deepest cavity	40 mm		
Fiber volume fraction	47 %	Maximum wall angle	40°		
Material bond	None	Tightest radius	20 mm		
Tensile strength	520 MPa				Varied
Youngs modulus	50 GPa				Determined
Storage condition	Ambient				Uncertainty

Table 3
Target variables analyzed and the associated method of assessment.

Primary/Formability		Secondary/Quality		Tertiary/Process	
Variable	Measured by	Variable	Measured by	Variable	Measured by
Tear	Visually	Surface quality	Visually	Forming forces	FTN-Omega-160/191
Wrinkling	Visually	Global geometric accuracy	3D-Scan		
Deconsolidation	Optical microscopy	Local geometric deviations	3D-Scan		
Delamination	Optical microscopy	Void geometry	Optical microscopy		
Metal tear	Visually	Matrix cracks	Optical microscopy		
Separator tear	Visually				Qualitative analysis
Separator wrinkling	Visually				Quantitative analysis

organosheet thickness of 0.6 mm. Overall, the measurements indicate satisfactory homogeneity. The subsequent cooling ramp showed predominantly exponential behavior, as expected for the passive cooling employed. The chamber temperature initially decreased more steeply and approached the layup temperature range around the 120-minute mark, about 30 min after the heating was turned off. All measurement points within the layup were below 100 °C at the 97-minute mark and below 60 °C after about the 125-minute mark. At the end of the recording period, after a total of 150 min and one hour after shutting off the heating, the temperature at all measurement points, including the chamber, had fallen below 50 °C.

The thermal camera images confirm the high degree of homogeneity. Fig. 11 shows three exemplary images at 1000 s intervals within the time period in which the chamber was at its target temperature. Each colored contour band represents a temperature interval of 6 °C. Just like the inside of the layup, the outside temperature continued to rise slightly even after the chamber had reached its target temperature. While the outer area of the layup continued to rise significantly, the area of the organosheet stayed within a 12 °C interval. The overall heat in the sheet showed a slight bias towards the top of the layup, which also manifested in the sheet area, although the difference from top to bottom of the organosheet area was minimal. There was no relevant left–right bias, and the distribution in the horizontal direction was very close to that in the vertical direction.

3.2. Force measurements

3.2.1. Measurement stability

The forces measured in X, Y, and Z directions during the stability experiment are shown in Fig. 12. In addition to the raw data, the plot shows a rolling mean filter with a window size of 2000 s to assess both local and overall force fluctuations caused by the heating and cooling system. A general drift in the force measurements was observed in all components during heating. This was most pronounced in the Z component, which drifted by almost 30 N. However, towards the end of the measurement, the forces approached a steady state with no significant drift. This suggests that the tool's temperature initially changed as the chamber heated up, then reached a steady state at which only the periodic deviations from the water-cooler's cooling cycle remained. These oscillations were also most pronounced in the Z component of the force and remained largely constant in both amplitude and period

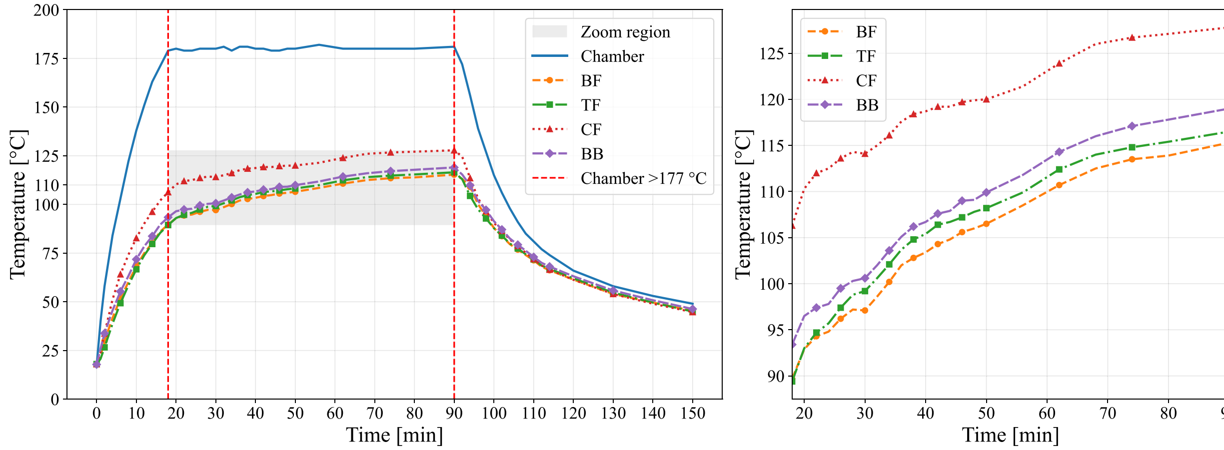

Fig. 10. Temperature in the heating chamber and at different layup locations (bottom front, top front, center front, bottom back) during heat-up, holding, and cool-down.

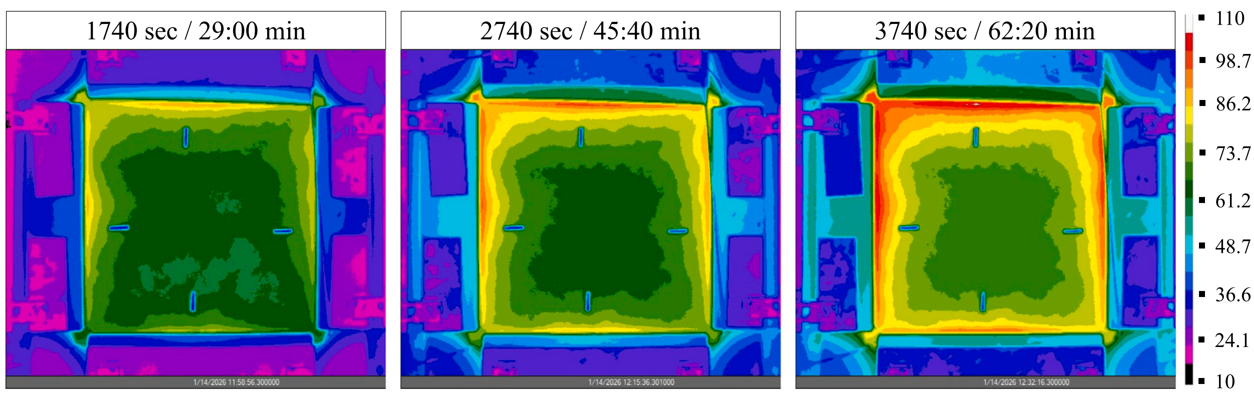

Fig. 11. Temperature distribution recorded by the infrared camera at 1740, 2740, and 3740 s after the start of the heat-up.

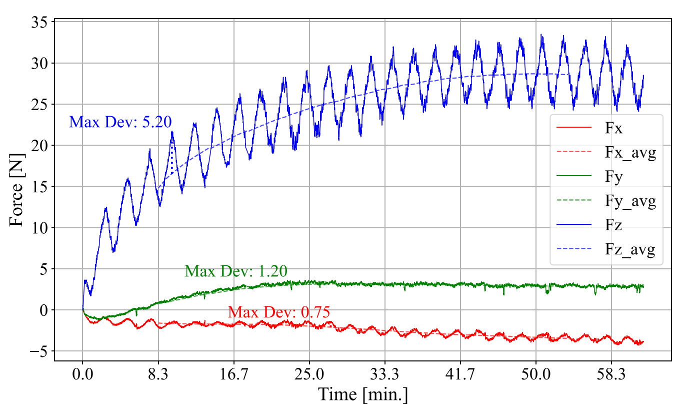

Fig. 12. Force components of the hot side force sensor during one hour after starting the heating system.

throughout the experiment. This oscillation had an amplitude of about ± 5 N and a period of about two minutes.

During manufacturing, the forces were set to zero at the beginning of the forming process. Therefore, most of the force deviation caused by its initial drift would be eliminated during the actual forming. The oscillation remains relevant, but its amplitude in the experiments was quite small relative to the target forces employed during forming (about 1%–5%), and its period of about two minutes was long compared to the frequencies relevant for the controller (up to 10 Hz). In conclusion, the oscillatory influence should be regarded as a reduction in the force sensor's accuracy, but it is unlikely to cause any major problems with the controller or the process.

3.2.2. *Force controller performance*

To assess the force controller performance, a spatial plot of the supporting robot TCP, colored by the support force, during the forming trial is shown in Fig. 13. Key performance metrics are listed in Table 4 alongside the results reported in [11], which were taken as a reference. Qualitatively similar force spikes associated with the shape's corners occurred, although they were especially pronounced in the latter half of the bottom right corner. In general, the force spikes and lows were far less pronounced than in the reference experiment, with only very few spikes reaching above 300 N, no spikes higher than 340 N, and no complete contact loss at any point. The comparison of performance metrics confirms the improved controller behavior, with about a 2.6-fold decrease in mean average error (MAE) and standard deviation (Std), as well as in the portion of force outside a ±50 N band around the target. Whether the observed performance increase was due to the different control approach, the lack of a stiffness compensation, different controller parameterization, or the differing robot setup cannot be concluded at this point. However, the experiment demonstrated the effectiveness of the implemented control scheme in keeping the support force close to the target and avoiding extreme force spikes.

3.2.3. *Support force*

For the analysis of the support force during FRTP forming, the second shape of experiment 10 shall serve as a representative example. As seen in Fig. 14, the force oscillated correctly around the target value of 200 N throughout the entire forming process. It mostly remained in

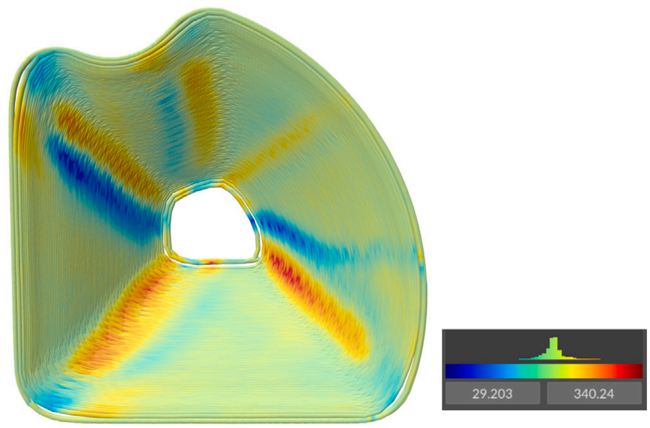

Fig. 13. Measured support force (in N) during the force controller performance assessment experiment, indicated by the color of the plotted global path of the support robot's TCP. The path is traversed outside-in in counterclockwise direction.

Table 4
Comparison of key force controller metrics between experiment 30 of Möllensiep et al. [11] and this work's replication (mean, mean average error (MAE), maximum and minimum measured forces (max, min), and standard deviation (std) in N, as well as percentage of measurements below 150 and 250 N).

	Mean	MAE	Max	Min	Std	F < 150	F > 250
Reference	199.99	49.84	779.32	−10.78	84.61	14.84	14.05
This work	198.24	19.18	340.24	29.20	32.28	5.34	5.26

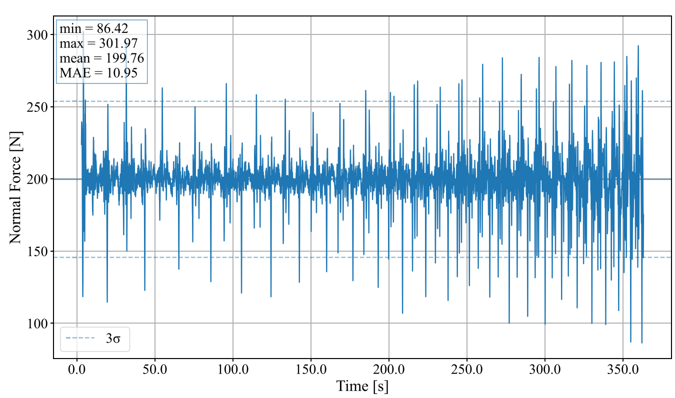

Fig. 14. Controlled normal force of the support robot during the elevation spiral strategy in the second intermediate shape of experiment 10.

a close interval around the target with an MAE of 10.95 N. Periodically, more pronounced spikes were observed, which reached up to a maximum of 302 N and a minimum of 86.42 N. The controller thus showed even better performance than in the previously reported experiment, which could be attributed to the absence of sharp corners in the formed geometry.

Fig. 15(a) shows a spatial plot of the relative position of the supporting robot's TCP with respect to the guiding tool, colored by the support force. The plot clearly shows that even without sharp corners, the spikes in the support force appeared at constant longitudes. This implies that they were not solely a result of the controller, but were caused by an underlying system property. It appears that the spikes resulted from a sudden change in the required distance to maintain the support force. This can also be seen in the detail view of Fig. 15(b), which shows the absolute position correction changing between distinct plateaus over time. The cause of such changes in distance levels could have been defects in the tool or sheet surfaces or, most likely, axis backlash, resulting in positional deviations.

As the diameter of the cone decreased with increasing depth, the force spikes had a higher frequency towards the end of the forming run. Due to the quicker change in the longitude of the support tool relative to the forming tool, the controller had less time to react to the sudden change of the required distance to maintain the target force. This shortened reaction time could explain the increase in magnitude of the peaks towards the end of the forming run. Another effect could be an increase in stiffness of the system due to material thinning with increasing forming depth. This is supported by the steadily increasing absolute correction over time in Fig. 15(b), which coincides with an increase in the peak amplitude. Comparing the absolute corrections at the beginning and the end of the forming path, the compensation of material thinning seems to have caused a necessary position adjustment of about a millimeter.

Compared to the elevation-based paths, the force measured in the same shape during geodesic paths in experiment 12 (Fig. 16) shows a significantly steeper increase towards the end. Forces in this last section reached as high as 390 N and in two cases even fell to zero. This behavior can be explained by the increasingly small circles the global geodesic path took at the tip of the cone. Because the speed was constant along the entire path, the period of the sudden force spikes decreased with the contour radius, and the controller therefore had less time to react to them.

Comparing the spiral strategies to the draping strategy in experiment 10 (Fig. 17), the maximum as well as the mean average error increased significantly, with spikes reaching up to 558 N and an MAE of 34.6 N. Here, the deviations were strongest at the beginning and decreased along the path. As detailed in Section 2.3, the draping path started with a cross running through the center of the cone. The initial movements, therefore, had the highest degree of deformation and spanned the greatest global distance. After some time, the paths no longer crossed the tip section of the cone, not only reducing the degree of deformation but also reducing the change in wall angle and in thickness covered by the path. This might explain why larger deviations were observed in the beginning. The higher overall deviations are likely due to the sharp corners in the paths and the greater thickness and angle gradients, even excluding the tip region. Additionally, the draping paths crossed over the grooves left by the previous spiral paths, which might also have contributed to the increased deviations.

Overall, the force controller successfully compensated for both material thinning and system inaccuracies during the actual FRTP forming. The deviations remained within an acceptable range, a loss of contact or dangerously high forces were effectively avoided, and the force was well controlled and remained very close to the target force. Further tuning of the control parameters might reduce peak forces, but will always result in a trade-off between the swiftness of the controller action and its peak deviation. A more comprehensive improvement could be achieved by identifying the precise cause(s) of the deviations and building a predictive model to be incorporated in the control pipeline.

3.2.4. Forming force

Regarding the forming force measured at the guiding robot, Fig. 18 shows the recorded absolute forces for the four elevation spiral paths of experiment 10. The forces measured in the first three shapes increased almost linearly with the path progress before dropping at the end. This final decrease began with the tip radius of the cone, where only a slight additional depth increase occurred, and ended with the support force of 200 N being removed at the very end of the shape. The maximum force towards the end of each intermediate shape's path increased from just over 600 N in the first shape to more than 1000 N in the second and more than 1200 N in the third. This correlates with the increase in the absolute forming depth with each intermediate shape. However, the maximum force measured in the last shape, which had the overall

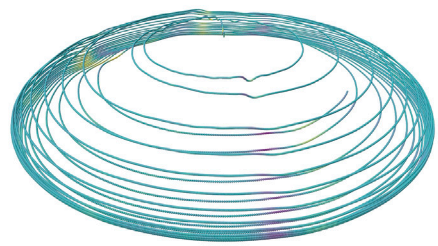

(a)

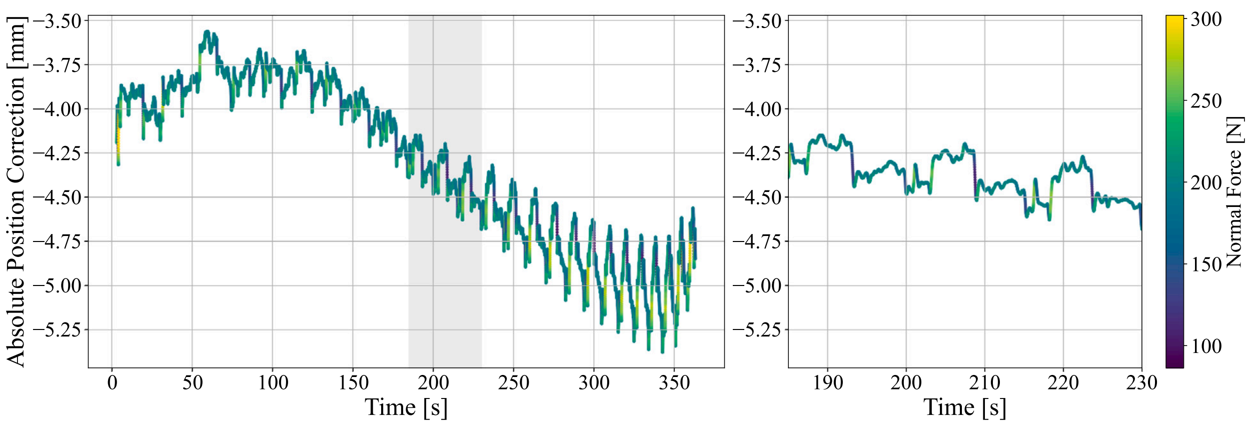

(b)

Fig. 15. Force-controlled support tool correction during an elevation-based spiral in the second shape of experiment 10: (a) relative support tool position, (b) absolute position correction with detail view.

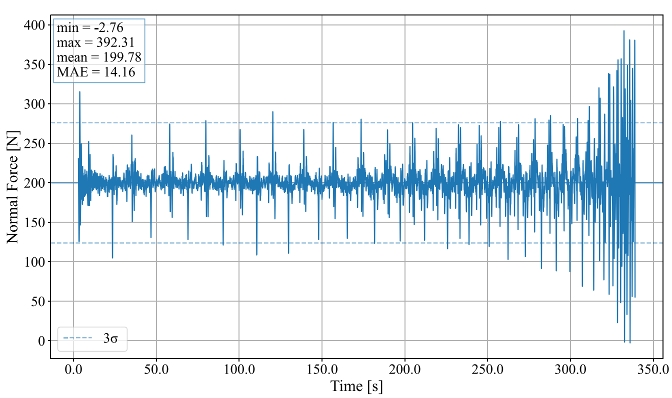

Fig. 16. Controlled normal force of the support robot during the geodesic spiral strategy in the second intermediate shape of experiment 12.

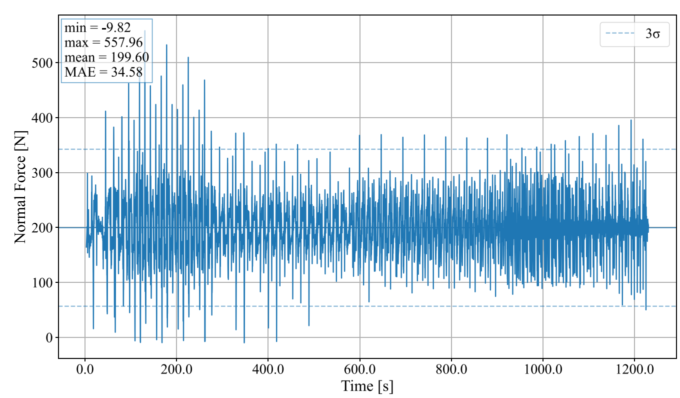

Fig. 17. Controlled normal force of the support robot during the fiber following path strategy in the fourth intermediate shape of experiment 10.

highest absolute forming depth, was just over 800 N. This indicates the influence of the relative depth increase, which was the lowest in the last shape, with just 3 mm compared to the preceding intermediate draping shape. Considering the support force contribution of 200 N and the elastic deformation component, the overall low force indicates that only minor plastic deformation occurred during this final shape. However, especially towards the beginning of the last shape, the force oscillations were comparably higher than in shapes one to three. This could also be attributed to the previous draping path, which left grooves in the metal sheet running orthogonally to the spiral path. Interestingly, the force of the last shape did not show the same linear increase as in the previous shapes. Instead, there was a significant increase towards the end. In the subsequent cooling run, where the same paths were repeated, the increase in force towards the end of the path was much less pronounced (see Fig. 19). This indicates that the deformation introduced during the draping pass had been largely removed by the last shape. However, during the remainder of the cooling run, the force was actually slightly higher than during the initial pass. This was likely due to increased layup stiffness resulting from cooling and solidification of the polymer matrix.

3.3. Forming strategy comparison

The results of the strategy comparison reveal the important contribution of both the intermediate shapes and the path planning strategy. While Figs. 20 and 21 present the 3D scans of the formed surfaces,

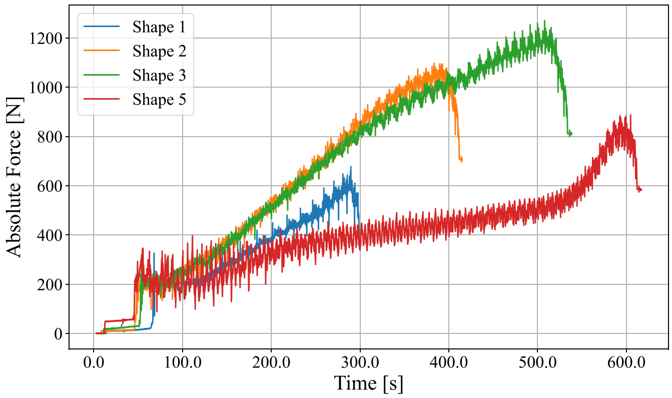

Fig. 18. Forming force during forming of four subsequent shapes of experiment 10.

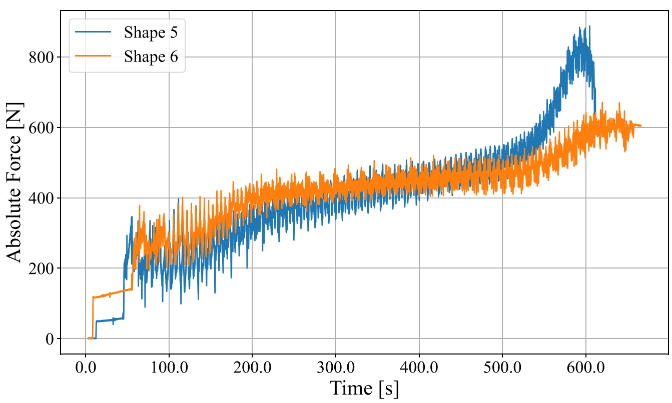

Fig. 19. Comparison of the forming force during the final shape and subsequent cooling run on the same geometry in experiment 10.

including geometric deviations, Table 5 lists the accuracy metrics of all trials. First, Fig. 20(a) and (b) shows the difference between a cone formed in a single stage and a cone formed in a multi-stage strategy, both with elevation-based spirals. Compared to the one-shot E40 strategy (experiment ID 03), the E10-E10-E10-E10 strategy with four intermediate shapes (ID 04), with a gradual increase in forming depth and wall angle, greatly reduced both the minimum and maximum geometric deviations and the standard deviation of the geometric deviations. Qualitatively, a significant underforming around the tip (negative values in geometric deviation) and overforming (positive values) around the base still occurred. The deviations, however, were much smaller and more localized in the multi-stage strategy than those in the drastically deviating E40 part. As also visible in the top-view images, wrinkling was qualitatively reduced as well, but radial wrinkles can still be clearly seen along the diagonal directions of the woven reinforcement.

The fiber-following draping toolpath strategy was developed to suppress these wrinkles. As Fig. 20(c) shows, introducing a draping toolpath for forming the last intermediate shape after three elevation-based spiral shapes (E12-E12-E12-D3, ID 05) successfully achieved a wrinkle-free result in the formed region of the sheet. Furthermore, under the investigated conditions, the overall part quality was increased, and the standard deviation and maximum deviation were significantly reduced compared to E10-E10-E10-E10. However, the vertical and horizontal directions of the sheet towards the tip were significantly underformed, which led to a visible deviation from circular to a square-shaped tip.

Table 5
Accuracy metrics of the performed experiments as listed in Table 1 (all metrics in mm).

ID	Min. Dev.	Max. Dev.	Std. Dev	Spread
01	−5.04	6.66	4.07	11.7
02	−4.68	7.37	4.24	12.05
03	−4.87	6.73	3.67	11.6
04	−3.18	3.66	1.97	6.84
05	−3.01	2.89	1.36	5.9
06	−3.40	3.72	1.48	7.12
07	−2.17	2.32	0.96	4.49
08	−2.14	2.69	1.29	4.83
09	−1.78	2.19	0.75	3.97
10	−1.54	1.5	0.77	3.04
11	−1.54	1.6	0.75	3.14
12	−1.12	1.52	0.66	2.64
13	−2.19	1.62	0.96	3.81
14	−1.92	2.8	0.95	4.72

Performing the draping toolpath with no nominal depth increase relative to the preceding intermediate shape (strategy E10-E10-E10-E10-D0, experiment 09) improved all accuracy measures. The underforming along the vertical and horizontal directions is still visible in Fig. 21(b), but it is much less pronounced compared to the E12-E12-E12-D3 strategy (experiment 06), shown in Fig. 21(a). The minimum deviation was reduced to −1.78 mm instead of −3.40 mm, and the standard deviation of 1.48 mm was almost halved to 0.75 mm. The result of the E10-E10-E10-E10-D0 part is wrinkle-free as well. Compared to E10-E10-E10-E10, this result suggests that the draping process during this shape progression might have reshaped the part, removing wrinkles introduced during the preceding shapes.

Another approach to reduce the radial underforming in the tip is the addition of a final spiral toolpath after the draping shape, as in strategy E12-E12-E9-D3-E3 of experiment 08, shown in Fig. 21(c). Following this approach, underforming was reduced, but to a lower degree than with ending on a D0 shape. Adding a cooling run in the E12-E12-E9-D3-E3-E0c strategy (ID 10) can be seen as a combination of both approaches: Spiral paths are employed in the final shape, which is then repeated without additional depth increase. Indeed, the geometric accuracy was further enhanced with this strategy, as depicted in Fig. 21(d). Some underforming at the tip and overforming at the base persisted, but the minimum and maximum deviations were reduced even below that of the E10-E10-E10-E10-D0 strategy. Using geodesic spiral paths rather than elevation-based spirals apparently reduced the underforming in the tip region, making G12-G12-G9-D3-G3-G0c, as performed in experiment 11, the qualitatively best of the tested strategies so far. As visible in Fig. 21(e), however, the maximum deviation at the base is slightly increased compared to the elevation-based approach.

Fig. 22 shows the final wrinkle-free cone with distinct base and tip regions in more detail. Draw-in of the sheet edges in the 0° and 90° directions is visible in Fig. 22(a), and noticeable shear deformation was introduced in the 45° direction as highlighted in detail (c). Remaining surface defects were the light impression of tool paths in the tip region (see Fig. 22(a)) and small imprints of wrinkles of the PTFE sheets, as shown in detail (d).

3.4. Parameter analysis

The limited extent of the experiments regarding the process parameters limits the generalizability of the findings, especially as the effects from the parameter choices are less qualitatively obvious than those of the strategies. Still, although no full parameter analysis was performed, some preliminary observations on parameter effects can be concluded from the experiments. The first such effect is that of increased temperature in the E40 strategy experiments (01 vs. 03), which improved the overall accuracy, although the spread was only marginally reduced, and overall deviations remained high even at

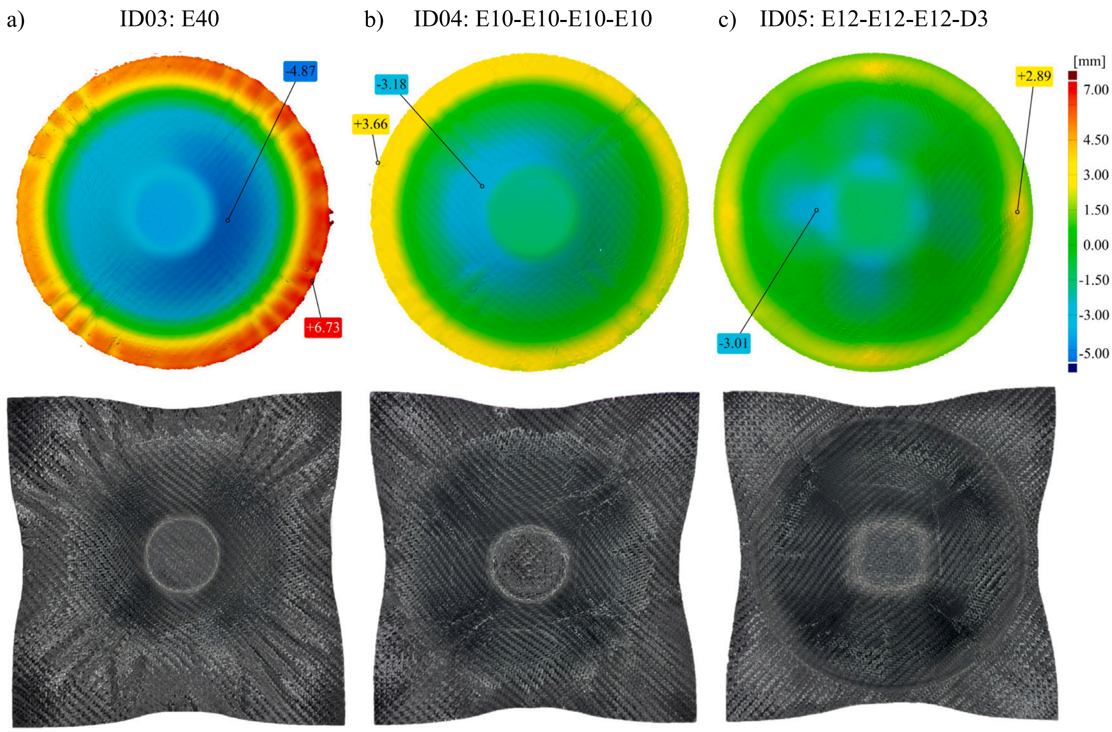

Fig. 20. Comparison of forming results of elevation-based single-stage strategy E40 (a), multi-stage strategy E10-E10-E10-E10 (b), and multi-stage strategy with draping pass (c). Top-view images and 3D scans with colors indicating geometric deviations from target geometry.

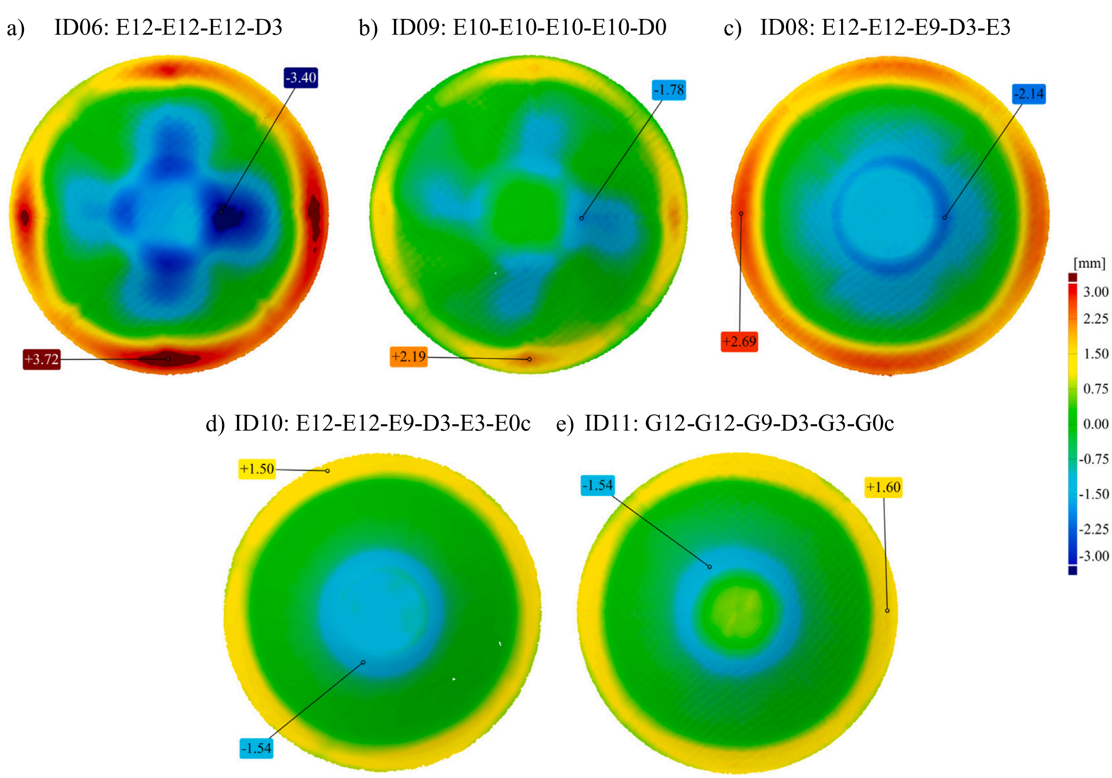

Fig. 21. Comparison of forming results of multi-stage strategies including elevation-based (E), geodesic (G), and draping (D) paths. 3D scans with geometric deviations of formed cones.

180 °C, owing to the single-stage approach. The improved accuracy was likely due to the softening of the matrix past its glass transition temperature, which likely reduced force-related robot displacement and improved the general formability of the composite.

Regarding the influence of the support force, first, experiments comparing SPIF (no support) and DSIF were conducted. In the E40 strategy, substantial reductions in the maximum and standard deviations were observed when employing DSIF (ID 03) instead of SPIF

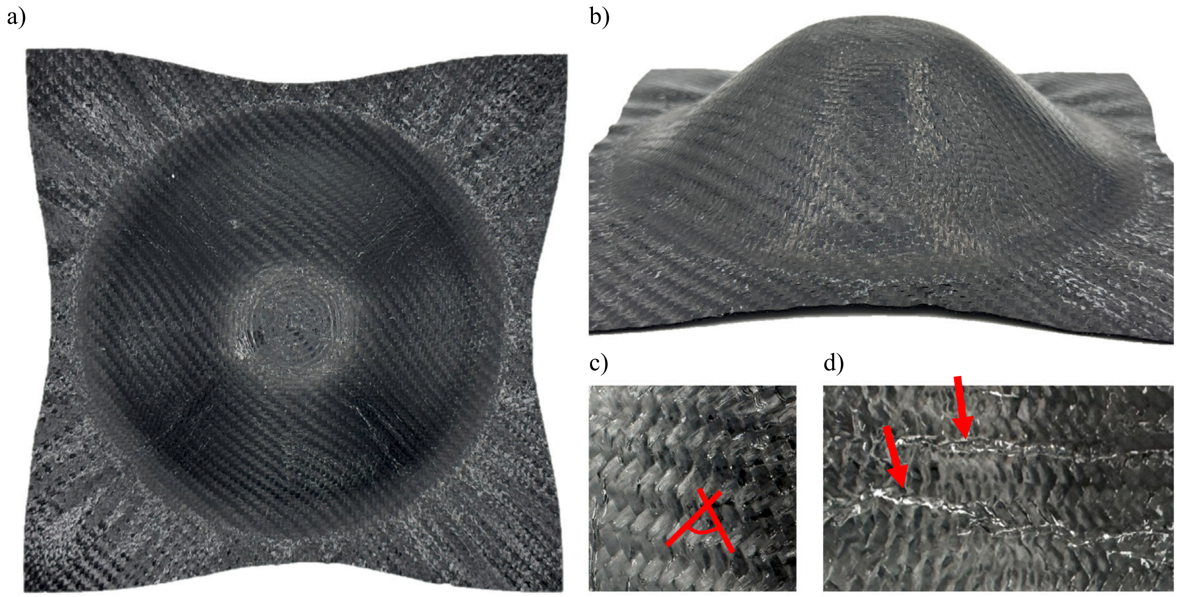

Fig. 22. Cone produced with the qualitatively best strategy G12-G12-G9-D3-G3-G0c in experiment 11. (a) Top view, (b) side view, (c) shear introduced between warp and weft yarns, (d) imprints of wrinkles of the PTFE sheets on the surface.

(ID 02). Furthermore, the span of the error was slightly reduced. Although the overall results were not satisfactory due to the single-stage approach, this provides a first indication of a positive effect of the supporting tool. The comparison of DSIF and SPIF at the G12-G12-G9-D3-G3-G0c strategy (experiment 13 vs. 14) shows high reductions in the maximum error and error spread, but the same standard deviations. However, in both strategies, the minimum deviation increased slightly when DSIF was used instead of SPIF. Therefore, the support tool's main impact on accuracy was in supporting the base in the transition zone between the formed geometry and the flat sheet. Interestingly, experiment 14 still shows a better accuracy than many of the other DSIF experiments, especially ID 01, ID 03, and ID 04, which again highlights the importance of the employed forming strategy. The strategies that performed best in the DSIF experiments also appeared to be beneficial for the SPIF process. Thus, within the tested conditions, a SPIF process with a more suitable combination of intermediate shapes and path strategies can outperform a DSIF process with a less suitable strategy. Increasing the support force from 150 N (ID 05) to 200 N (ID 06) worsened all accuracy measures. This is contrary to the expectation that an increased support force would help to further localize deformation and reduce the gap between the dummy sheets. The deviations of the 200 N specimen show a stronger asymmetry than those of any of the other experiments, which could indicate a process error skewing the results. It could also be that the increase in force actually reduced accuracy through stronger elastic deformation of the guiding robot, but this seems unlikely considering the extent of the force increase and the estimated robot stiffness, which would only account for an increase of about 0.1 mm.

Using an aluminum sheet (ID 07) in the front rather than a steel sheet (ID 06) had a strong positive effect on all accuracy metrics in this study. One possible explanation could be the lower flow stress and, therefore, smaller elastic component of the deformation, as well as lower forming forces, which could have reduced robot deflection and springback. However, a slight increase in roughness at the initial cross of the draping path was qualitatively observed. These toolpath imprints on the FRTP surface are favored by the soft aluminum, which plastically deforms easily around the tooltip. It is also important to note that the high forces on the side of the guiding tool resulted in significant abrasion of the soft aluminum sheet. Still, from these initial results, this dummy sheet configuration appears to be a promising alternative to the steel-aluminum setup and warrants further investigation, particularly with a rotating or roller-ball tool, which could reduce abrasion. Contrary to initial expectations, increasing the contour distance to 3 mm within the G12-G12-G9-D3-G3-G0c strategy (experiment 12 vs. 11) improved the accuracy measures, particularly the error spread. An increase in surface roughness was qualitatively not observed, making experiment 12 the one with the best results. Another increase in the contour distance to 5 mm (experiment 13) resulted in clearly visible imprints of the toolpaths on the organosheet surface, particularly in the tip section of the cone frustum. Additionally, a contour distance of 5 mm resulted in lower overall part accuracy than the 3 mm trial. This could be attributable to the lower geometric resolution, which becomes more pronounced as it approaches a larger fraction of the vertical arc length. The contour distance is one of the most important contributors to forming time. While the results of experiment 13 indicate that very high distances decrease geometric accuracy and surface quality, those of experiment 12 imply that a certain increase is at least not detrimental and might even improve the outcome. Therefore, further research will be required to more precisely gauge the influence of the contour distance on the forming accuracy, thereby minimizing forming time while maintaining sufficient accuracy and surface quality.

Overall, in this study, the process parameters within the chosen ranges had a less substantial influence on the process outcome than the chosen strategy. Further research will be necessary to confirm the generalizability of the observed effects and to investigate parameter interactions. The overall progress achieved during the investigations, including strategies and parameters, is shown in Fig. 23. Starting from the low accuracy, strongly wrinkled E40 part at low temperature (a), intermediate shapes at an increased temperature (b) already greatly improved accuracy and reduced wrinkling. The addition of fiber-following paths (c) eliminated the remaining wrinkles and led to good general accuracy, which was further increased by using an aluminum sheet. The best tested strategy G12-G12-G9-D3-G3-G0c, with slightly increased contour distance (d), resulted in a wrinkle-free, well-shaped part with greatly improved accuracy.

To further validate the optimal parameter combination and assess process repeatability, experiment 15 was conducted. From the results so far, the best theoretical parameter combination appears to be the G12-G12-G9-D3-G3-G0c strategy, an aluminum front sheet, a force of 150 N, a temperature of 180 °C, and a contour distance of 3 mm.

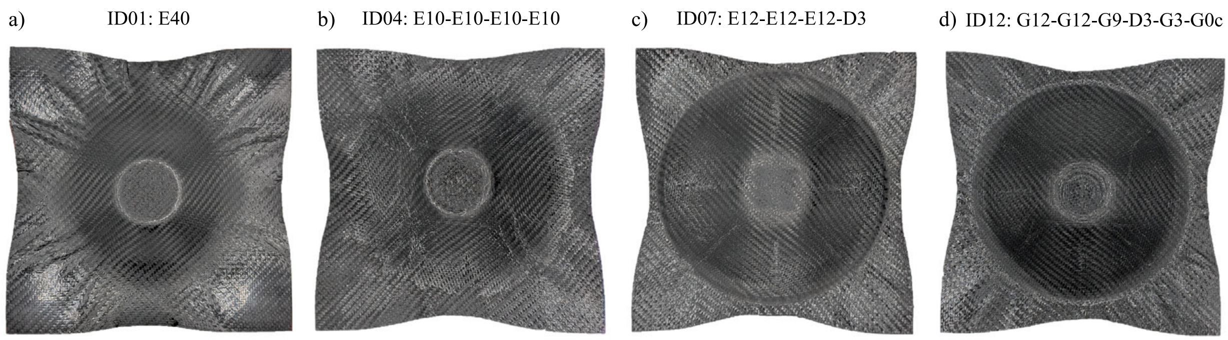

Fig. 23. Top-view images for comparison of forming results of (a) single stage elevation spiral strategy at reduced temperature, (b) multi-stage strategy with four intermediate shapes, (c) elevation spirals and final draping pass with two aluminum sheets, and (d) one of the best tested strategies with geodesic spirals following the draping pass and increased step size.

This parameterization was used to carry out experiment 15 three times. The quantitative results are shown in Table 6. The results indeed show the lowest maximum deviation and the lowest standard deviation of all experiments. The spread and minimum deviation are second best after experiment 12 and are close to those of experiments 10 and 11. Experiments 12 and 15 differ only in force and front sheet, suggesting a negative interaction between these parameters regarding the minimum deviation, but further research will be necessary to confirm or disprove this. For now, the results of experiments 10, 11, 12, and 15 are overall very similar and therefore do not allow a definitive conclusion. Concerning the observed repeatability of experiment 15, the standard deviations calculated from the three repetitions range from 0.06 mm to 0.03 mm, depending on the accuracy metric. Considering the repeatability of the robots and possible variations during the manual layup and clamping process, experiment 15 shows a good repeatability of the process under the tested parameterization and experimental conditions. However, especially with the manual layup and clamping process currently employed, the operator becomes a significant factor to consider in the repeatability. The three experiments performed here were carried out by the same operator on two consecutive days. The repeatability might therefore be lower when different operators perform experiments and when there is a longer time between experiments. Furthermore, repeatability will likely suffer significantly when studying parameter ranges that do show wrinkling in the formed region due to the variance in exact wrinkle manifestation. Still, the results show that with a suitable strategy, parameter choice, and consistent operator, the process can already achieve good robustness. While this is definitely a favorable property, it is nonetheless unlikely that the discovered parameter combination already represents the ideal one. It rather forms a robust reference for further investigation and improvement. Determining the actual best parameterization will require significant further research: Parameter influences and their interactions should be quantified through proper statistical design of experiments, the varied parameter space should be extended significantly to include further influences, and the process repeatability should be further ensured and improved, for example, by assisting or automating the currently manual procedures.

3.5. Failure modes and consolidation state

Within the scope of the performed experiments, wrinkling constituted the only relevant failure mode that determined the formability of the cone geometry. The combination of multi-stage forming and fiber-following paths could successfully prevent the wrinkling of the organosheet in the investigated cone geometry. Wrinkling of the PTFE separator sheets could not be prevented, which was likely caused by a combination of the PTFE's low bending stiffness and the non-uniform stretching introduced during the forming process. These wrinkles were then imprinted into the surface of the organosheets by the applied tool pressure and led to the surface defects seen in Fig. 22(d). While these defects occurred to an extent that reduced surface quality, they remained superficial and were not considered a limit on formability in this study. None of the constituents (dummy sheets, organosheets, and PTFE separators) failed by tearing in any of the experiments. However, this failure mode is likely to occur at more demanding strategies and geometries for the clamped dummy sheets and separators, as seen in [28].

Table 6
Accuracy metrics of experiment 15 with strategy G12-G12-G9-D3-G3-G0c, an aluminum front sheet, a force of 150 N, a temperature of 180 °C, and a contour distance of 3 mm (all metrics in mm).

ID	Min. Dev.	Max. Dev.	Std. Dev.	Spread
15.1	−1.49	1.35	0.59	2.84
15.2	−1.59	1.36	0.62	2.95
15.3	−1.48	1.41	0.55	2.89
Mean	−1.52	1.37	0.59	2.89
Std. Dev.	0.06	0.03	0.04	0.06

In the cross-sectional micrographs, qualitative differences between the virgin and incrementally formed material are visible, as shown in Fig. 24. The shown micrographs illustrate representative sections of the 27–30 mm long samples that were investigated. In the virgin material micrographs, longitudinal cracks were observed that run through both the matrix-rich regions and the fiber bundles, spanning over 2 mm in length. These cracks were present throughout almost the entirety of the two samples taken from different virgin material sheets and were therefore likely present in most of the used material. Notably, these cracks were almost entirely absent in all of the formed samples. Cracks still appeared, as seen in the micrograph of the base sample of the experiment 11 strip. However, they occurred way less frequently and were significantly reduced in both length and width. However, there were still notable voids in the formed cross sections. All of the observed voids had an elliptical shape and appeared exclusively in the matrix-rich regions of the ply. The void area for the experiment 11 samples ranged from the largest pore observed in the base micrograph (0.041 mm^2) to medium and small voids with areas in the realm of 0.005 to 0.01 mm^2. Entirely void-free sections were also observed, as exemplified by the wall micrograph. The samples for experiment 3 also showed elliptical voids in the matrix-rich regions, although they were much more frequent, spread throughout the samples, and larger. Comparing the samples, it appears that the overall consolidation was improved by the forming process relative to the virgin material. In general, the longitudinal cracks in the virgin material were greatly reduced or even eliminated. This is likely attributable to the forming and support forces acting perpendicularly to the cracks, compressing and closing them. The elliptical voids, on the other hand, were not previously present in the virgin material and therefore must have emerged

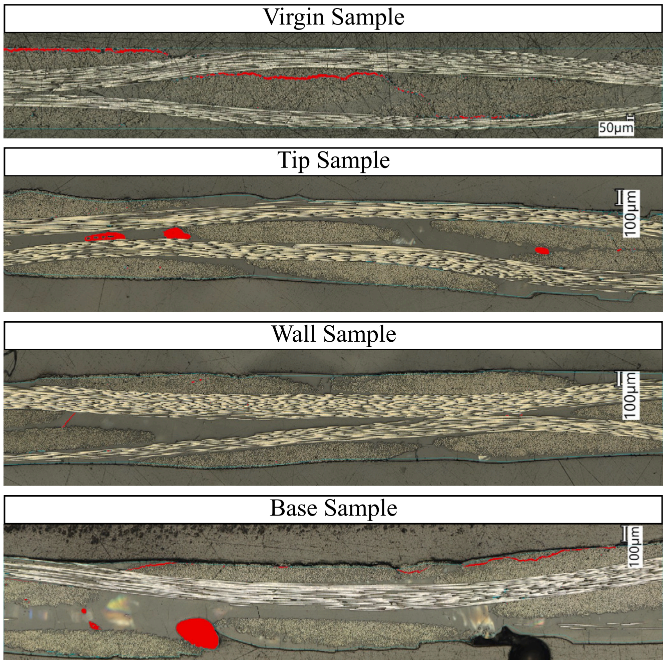

Fig. 24. Micrographs of cross-sections taken from three locations of the part formed with the parameters of experiment 11 and of a piece of virgin material, with voids and cracks highlighted in red.

during the process. Their elliptical form and their occurrence in matrix-rich regions indicate that they may have resulted from gas expansion. One possible explanation is the expansion of bound water absorbed by the polymer during storage, as the organosheets were shelf-stored and not dried before the forming experiments. Delamination was not observed in any of the samples.

4. Conclusion and outlook

This work presented the double-sided incremental forming of continuous fiber reinforced thermoplastic sheets into a cone frustum geometry. The process analysis revealed that the purpose-built DSIF system enables homogeneous global heating of the organosheet, albeit with a significant gradient between the chamber and the sheet temperatures. It also showed that, for the investigated material system and parameter range, the ISF process was already feasible at temperatures lower than those typically used in conventional thermoforming. The employed force sensor was not significantly affected by the heating and cooling system. However, when forming at low support forces, its influence might become more relevant. Overall, the relative force controller with geometrically coupled robots performed well when compared to the alternative absolute implementation. Local force peaks were rare and non-critical. Still, future research should investigate the causes of the force spikes and explore options to further suppress them. The measured forming forces make a relevant deflection of the frame unlikely. However, a displacement of the guiding robot is very likely, which motivates the future implementation of a stiffness compensation scheme to improve the geometric accuracy of the final parts. For the investigated geometry and material, the strategy investigations showed that combining intermediate shapes with different path strategies is crucial for achieving high-quality results. The use of multiple intermediate shapes on its own already greatly improved the part quality. With the introduction of a draping toolpath shape, wrinkling was eliminated within the formed region across all tested strategies. Finishing spiral toolpaths were able to redress the orthogonal underforming introduced by the draping shape. Geodesic spirals instead of elevation spirals mitigated underforming in the flat-tip region of the cone. While macroscopic failure modes such as tearing and wrinkling were effectively prevented for the investigated process conditions, some microscopic defects remained in the base and tip regions of the formed parts. Future investigations should address these defects by drying the semi-finished product prior to incremental forming and, if necessary, increasing support forces in critical regions.

While cone frustums with high quality were already achievable with the identified strategies, future research should investigate how many shapes are truly necessary and whether early shapes can be formed with increased contour distances to reduce the processing time. A more advanced processing pipeline should use heuristics, simulation, or machine learning to automatically create intermediate shapes for a given input geometry that maximize formability, quality, and process performance. To enable this, the dominant deformation mechanisms of the FRTP during DSIF must be thoroughly identified, and a quantitative relationship between forming strategies and those deformation mechanisms must be established. This requires a time-resolved analysis of the shear angle distribution, fiber draw-in, and interply shear, among others. Another avenue for future research is the investigation of more complex and demanding target geometries. An initial application of the developed forming strategy to more complex geometries with varying wall angles and asymmetries already showed promising results, as reported by the authors in [36]. However, fabricating larger parts remained challenging, and smaller corner radii, concave-convex elements, and parts with multiple features will likely pose additional challenges. Addressing these will require further investigations and adaptation of forming strategies.

Concluding the present study, the final results already show a qualitatively satisfactory process for the investigated FRTP material and cone geometry. No detrimental defects or major shape deviations were observed in the final strategy and parameter configurations. It is now the task of future investigations to further push the capabilities, geometric accuracy, and speed of the process. One contribution will be the adoption of measures such as stiffness compensation and roller-ball tools from metal ISF. Another major contribution will be the continued optimization of process parameters and strategies. However, the present results already demonstrate that the DSIF of continuous fiber reinforced thermoplastics is feasible under the investigated conditions and can yield parts with a quality approaching that observed in metal ISF.

CRediT authorship contribution statement

Doran Nettig: Writing – review & editing, Writing – original draft, Visualization, Validation, Software, Investigation, Conceptualization. **Jan-Erik Rath:** Writing – review & editing, Writing – original draft, Visualization, Validation, Investigation, Conceptualization. **Jon Ove Tiedemann:** Visualization, Investigation, Data curation. **Thorsten Schüppstuhl:** Supervision, Resources, Project administration, Funding acquisition.

Funding

This work was supported by the German Federal Ministry for Economic Affairs and Energy [grant number 20Q1917C].

Declaration of competing interest

The authors declare that they have no known competing financial interests or personal relationships that could have appeared to influence the work reported in this paper.

Data availability

Data will be made available on request.

References

[1] Estin & Co, Lucintel. JEC observer: Overview of the global composites market 2024–2029. JEC composites magazine; 2025, Special issue.

[2] Neitzel M, Mitschang P, Breuer U. Handbuch verbundwerkstoffe: Werkstoffe, verarbeitung, anwendung, 2nd ed., aktualisierte und erweiterte Auflage ed.. Hanser eLibrary, Hanser, München; 2014, http://dx.doi.org/10.3139/9783446436978.

[3] Al-Obaidi A, Kunke A, Kräusel V. Hot single-point incremental forming of glass-fiber-reinforced polymer (PA6GF47) supported by hot air. J Manuf Process 2019;43:17–25. http://dx.doi.org/10.1016/j.jmapro.2019.04.036.

[4] Leszak E. Apparatus and process for incremental dieless forming. 1967.

[5] Jeswiet J, Micari F, Hirt G, Bramley A, Duflou J, Allwood J. Asymmetric single point incremental forming of sheet metal. CIRP Ann 2005;54(2):88–114. http://dx.doi.org/10.1016/S0007-8506(07)60021-3.

[6] McAnulty T, Jeswiet J, Doolan M. Formability in single point incremental forming: A comparative analysis of the state of the art. CIRP J Manuf Sci Technol 2017;16:43–54. http://dx.doi.org/10.1016/j.cirpj.2016.07.003.

[7] Attanasio A, Ceretti E, Giardini C. Optimization of tool path in two points incremental forming. J Mater Process Technol 2006;177(1–3):409–12. http://dx.doi.org/10.1016/j.jmatprotec.2006.04.047.

[8] Malhotra R, Cao J, Ren F, Kiridena V, Cedric Xia Z, Reddy NV. Improvement of geometric accuracy in incremental forming by using a squeezing toolpath strategy with two forming tools. J Manuf Sci Eng 2011;133(6). http://dx.doi.org/10.1115/1.4005179.

[9] Ullah S, Xu P, Li X, Li Y, Han K, Li D. A review on part geometric precision improvement strategies in double-sided incremental forming. Metals 2022;12(1):103. http://dx.doi.org/10.3390/met12010103.

[10] Meier H, Smukala V, Dewald O, Zhang J. Two point incremental forming with two moving forming tools. Key Eng Mater 2007;344:599–605. http://dx.doi.org/10.4028/www.scientific.net/KEM.344.599.

[11] Möllensiep D, Gorlas T, Kulessa P, Kuhlenkötter B. Real-time stiffness compensation and force control of cooperating robots in robot-based double sided incremental sheet forming. Prod Eng 2021;15(5):683–99. http://dx.doi.org/10.1007/s11740-021-01052-4.

[12] Franzen V, Kwiatkowski L, Martins P, Tekkaya AE. Single point incremental forming of PVC. J Mater Process Technol 2009;209(1):462–9. http://dx.doi.org/10.1016/j.jmatprotec.2008.02.013.

[13] Marques TA, Silva MB, Martins PAF. On the potential of single point incremental forming of sheet polymer parts. Int J Adv Manuf Technol 2012;60(1–4):75–86. http://dx.doi.org/10.1007/s00170-011-3585-y.

[14] Zhu H, Ou H, Popov A. Incremental sheet forming of thermoplastics: a review. Int J Adv Manuf Technol 2020;111(1–2):565–87. http://dx.doi.org/10.1007/s00170-020-06056-5.

[15] Davarpanah MA, Zhang Z, Bansal S, Cao J, Malhotra R. Preliminary investigations on double sided incremental forming of thermoplastics. Manuf Lett 2016;8:21–6. http://dx.doi.org/10.1016/j.mfglet.2016.05.003.

[16] Hou C, Su X, Peng X, Wu X, Yang D. Thermal-assisted single point incremental forming of jute fabric reinforced poly(lactic acid) biocomposites. Fibers Polym 2020;21(10):2373–9. http://dx.doi.org/10.1007/s12221-020-1016-0.

[17] Lu B, Fang Y, Xu DK, Chen J, Ai S, Long H, Ou H, Cao J. Investigation of material deformation mechanism in double side incremental sheet forming. Int J Mach Tools Manuf 2015;93:37–48. http://dx.doi.org/10.1016/j.ijmachtools.2015.03.007.

[18] Okada M, Kato T, Otsu M, Hidetake T, Miura T. Development of optical-heating-assisted incremental forming method for carbon fiber reinforced thermoplastic sheet—Forming characteristics in simple spot-forming and two-dimensional sheet-fed forming. J Mater Process Technol 2018;256:145–53. http://dx.doi.org/10.1016/j.jmatprotec.2018.02.014.

[19] Lim T-C, Ramakrishna S. Modelling of composite sheet forming: a review. Compos Part A: Appl Sci Manuf 2002;33(4):515–37. http://dx.doi.org/10.1016/S1359-835X(01)00138-5.

[20] Fiorotto M, Sorgente M, Lucchetta G. Preliminary studies on single point incremental forming for composite materials. Int J Mater Form 2010;3(S1):951–4. http://dx.doi.org/10.1007/s12289-010-0926-6.

[21] Xiao X, Kim J-J, Oh S-H, Kim Y-S. Study on the incremental sheet forming of CFRP sheet. Compos Part A: Appl Sci Manuf 2021;141:106209. http://dx.doi.org/10.1016/j.compositesa.2020.106209.

[22] Xu P, Li X, Feng F, Li X, Yang Y. Experimental and numerical studies on two-point incremental forming of woven fabric composite sheet. J Manuf Process 2023;85:205–15. http://dx.doi.org/10.1016/j.jmapro.2022.11.049.

[23] Emami R, Mirnia MJ, Elyasi M, Zolfaghari A. An experimental investigation into single point incremental forming of glass fiber-reinforced polyamide sheet with different fiber orientations and volume fractions at elevated temperatures. J Thermoplast Compos Mater 2022;36(5):1893–917. http://dx.doi.org/10.1177/08927057221074266.

[24] Mirnia Kalaei SM, Razbin M, Emami M, Gholami MR, Salehian M, Biglari FR. Analysis of single-point warm incremental forming for glass fiber-reinforced polyamide 6 sheets: Experimentation and simulation. J Thermoplast Compos Mater 2024. http://dx.doi.org/10.1177/08927057241255884.

[25] Ambrogio G, Borda F, Conte R, Filice L, Gagliardi F. Processing of sheets made of long fibers reinforced plastics by SPIF. In: Material forming: ESAFORM 2024. Materials research proceedings, Materials Research Forum LLC; 2024, p. 1536–43. http://dx.doi.org/10.21741/9781644903131-170.

[26] Skjoedt M, Hancock MH, Bay N. Creating helical tool paths for single point incremental forming. Key Eng Mater 2007;344:583–90. http://dx.doi.org/10.4028/www.scientific.net/KEM.344.583.

[27] Hancock SG, Potter KD. The use of kinematic drape modelling to inform the hand lay-up of complex composite components using woven reinforcements. Compos Part A: Appl Sci Manuf 2006;37(3):413–22. http://dx.doi.org/10.1016/j.compositesa.2005.05.044.

[28] Rath J-E, Schüppstuhl T. Tool path strategies for single point incremental forming of fiber-reinforced thermoplastic sheets. In: Material forming: ESAFORM 2024. Materials research proceedings, Materials Research Forum LLC; 2024, p. 641–50. http://dx.doi.org/10.21741/9781644903131-71.

[29] Nettig D, Rath J-E, Kipping J, Schüppstuhl T. Instant geodesic draping for optimization and path-planning and its application to incremental composite sheet forming [preprint]. 2026, http://dx.doi.org/10.2139/ssrn.6553829.

[30] Xu P, Li X, Li X, Wang Y, Zhang W, Dong H, Zhi Q. Defects in double-sided incremental forming of woven fabric prepreg: experimental and numerical analysis. Thin-Walled Struct 2025;113229. http://dx.doi.org/10.1016/j.tws.2025.113229.

[31] Nettig D, Rath J-E, Schüppstuhl T, Frank J, Riecken B, Keun C-A. Hot double sided incremental forming of continuous fiber reinforced thermoplastics: Process analysis and system design. In: Material forming: ESAFORM 2026. Materials research proceedings, Materials Research Forum LLC; 2025, p. 1267–76. http://dx.doi.org/10.21741/9781644903599-138.

[32] Lu B, Chen J, Ou H, Cao J. Feature-based tool path generation approach for incremental sheet forming process. J Mater Process Technol 2013;213(7):1221–33. http://dx.doi.org/10.1016/j.jmatprotec.2013.01.023.

[33] Feng N, Crane K. A heat method for generalized signed distance. ACM Trans Graph 2024;43(4):1–19. http://dx.doi.org/10.1145/3658220.

[34] Crane K, Weischedel C, Wardetzky M. Geodesics in heat: A new approach to computing distance based on heat flow. ACM Trans Graph 2009.

[35] Nettig D, Rath J-E, Kipping J, Schüppstuhl T. Classifying parameters and target variables in incremental sheet forming of fiber reinforced polymers. Solid State Phenom 2026;389:11–25. http://dx.doi.org/10.4028/p-8f1QUK.

[36] Rath J-E, Nettig D, Schüppstuhl T. Hot double-sided incremental forming of fiber-reinforced thermoplastics: Process capabilities and challenges. Solid State Phenom 2026;389:1–9. http://dx.doi.org/10.4028/p-u5oc0K.